Observations of the Roots of Plasma Bubbles: Are they sometimes foamy?

Charles Lougheed Bennett[1]

[1]Lawrence Livermore National Laboratory (retired)

May 25, 2023

Observations of the Roots of Plasma Bubbles: Are They Sometimes Foamy?

Charles L. Bennett[1]

[1]Lawrence Livermore National Laboratory (retired).

Corresponding author: Charles Bennett (Charlie_Bennett@comcast.net)

Key Points:

- Dispersionless, highly attenuated, lightning generated electromagnetic waves are observed in the lower ionosphere
- The propagation of these electromagnetic waves has characteristics of acoustic wave propagation through two-phase foams
- Such foamy plasma bubbles may cover approximately 80% of the bottomside of the equatorial nightside ionosphere.

Abstract

Dramatic irregularities in the plasma density of the ionosphere, first discovered by their effects on radio wave propagation in 1938, and despite decades of investigation, still remain puzzling. Their deleterious effects on radio wave communication, satellite command and control, GPS navigation are serious enough to strongly motivate better understanding of their nature. Many aspects of such irregularities are now understood, but the mechanism(s) of their formation and their detailed nature remain a topic of great interest. In this work, detailed time resolved measurements of lightning generated waves show dispersionless, strongly attenuated propagation with substantial propagation delays. These characteristics of the electromagnetic wave propagation in the two-phase bubble/non-bubble ionosphere parallel the characteristics of acoustic wave propagation through two-phase liquid/vapor foams; and this motivates the suggestion that the bottomside layer of the ionosphere may sometimes be foamy.

Plain Language Summary

Just as ocean waves breaking at the interface between sea and land produce copious bubbles and foam, recent satellite data suggests a similar phenomenon at the interface between neutral atmosphere and the charged plasma of the ionosphere. Lightning generated electromagnetic waves passing through the lower ionosphere observed by low altitude satellites are found to have the same characteristics as acoustic waves passing through foamy water. This hypothetical foam in the lower ionosphere apparently strongly absorbs radio waves and seems to prevent most such waves from escaping the foam to pass through to the upper ionosphere.

1 Introduction

This article is a sequel to (Bennett, 2023), that describes a novel method for the observation and analysis of the *roots* of equatorial plasma bubbles (EPBs). Most of the details in (Bennett, 2023) will not be repeated here, but a brief summary is presented in the following section 2.

EPBs are localized density depletions (sometimes by over four orders of magnitude relative to the surrounding plasma) in the nighttime equatorial ionosphere (Heelis, 2004; Kil & Heelis, 1998; Woodman & Hoz, 1976). The literature on EPBs is vast and spans nearly a century. Nowadays there is increasing motivation to understand such bubbles and their detrimental affects on radio communications, especially satellite communications, for which “loss of lock” events can be precipitated by their presence. Another detrimental effect is the disruption of signals from the Global Navigation Satellite System so important to modern society. Numerous reviews of the development of the experimental and theoretical understanding of plasma bubbles are available (e.g. Balan et al., 2018; De Michelis et al., 2021; Huba, 2023; Kelley et al., 2011; Makela & Otsuka, 2012; Woodman, 2009).

It is generally accepted that the lower density of plasma bubbles relative to their surroundings causes them to rise in a turbulent process giving rise to plumelike features in radar observations (e.g. Abdu et al., 2012; Hysell et al., 2005; Kelley et al., 2011; Kudeki & Bhttacharyya, 1999; Narayanan et al., 2014; Patra et al., 2005; Tsunoda, 1983; Yokoyama et al., 2011). Plasma bubbles may also be detected as emission depletion bands in optical observations, (e.g., Immel et al., 2003; Kil et al., 2004; Makela & Kelley, 2003; Makela et al., 2006; Makela & Miller, 2008; Martinis et al., 2003; Mendillo & Baumgardner, 1982; Pimenta et al., 2003; Shiokawa et al., 2004). Animations of sequences of optical images, such as those in Makela and

Miller (2008) most clearly and dramatically show plasma bubbles emerging from low altitudes with subsequent rising and Eastward drifting. Such animations not only show apparent turbulent structures emerging from regions of depleted emission, but also show apparently non-turbulent depleted emission regions extending continuously below the turbulent regions towards the base of the ionosphere. In the present article the term *roots* of plasma bubbles refers to density depletions that extend *contiguously* to the base of the ionosphere that aren't necessarily turbulent. It is beyond the scope of this article to explain exactly how these density depletions are formed.

Initial observations and most early investigations of plasma bubbles involved so-called "spread F" phenomena, in which radar pulses of a given frequency, rather than reflecting from distinct ionospheric layers corresponding to distinct altitudes of reflection were observed to return from a spread out region of altitudes (Woodman, 2009). As such radar reflections require the presence of ionospheric density irregularities at the scale of the radar wavelength, conventional spread F phenomena would not be seen for non turbulent roots of plasma bubbles.

Woodman (2009) states "We implicitly assume that there is a cascade mechanism as proposed by Haerendel (1973) from the larger to the smaller scale, but we do not know exactly how this takes place." Woodman (2009) further states "The current state of the theory is that high frequency drift instabilities can explain the shortest wavelengths, up to ~1 m and the low frequency waves longer than 10 m, but no existing theory can explain the waves around 3 m, i.e., the strong echoes that Jicarmarca sees!"

Kelley (2011) states "How structure can be transferred from 1000 km to 1 m is still a bit of a mystery. Since there is linear growth in the power law regime, it is not because of an inertial cascade" and "Much remains to be done before the electrodynamics and coupling processes in this region during solar minimum conditions are fully understood."

To this day, the formation of the initial density depletions evidently required to "seed" larger scale turbulent fluctuations responsible for the greatest degradations of radio communications are not fully understood (Chou et al., 2022; De Michelis et al., 2022; Huba, 2023; Kil et al., 2022).

The remainder of this paper is organized as follows: Section **2** provides a summary of the earlier (Bennett, 2023) paper involving the detailed description of the data sources and analysis methods relevant to the current work. The main new results in the current work involve the detailed wavevector analysis of both dispersed (i.e. whistlers) and unusually low dispersion waves. In addition, previously unnoticed "precursors" to the ususually low dispersion whaves are identified and described. Normally dispersed waves are discussed in section **3**. In section **4** unusually low dispersion waves are discussed. Section **5** presents a physical model for "foamy" plasma. The various observations in (Bennett, 2023) and the new observations in the present paper are interpreted in terms of this model. Section **6** provides further discussion and conclusions.

2 Highlights of Earlier Work and New Observations

In (Bennett, 2023) I suggested that the roots of plasma bubbles might sometimes be foamy. This suggestion was made based on the propagation characteristics of lightning generated (LG) waves passing through such roots and in analogy to the propagation of acoustic waves through mixed liquid/gas phase foamy media. A specific model of the propagation of electromagnetic waves through such "plasma foam" at the bottom of the ionosphere will be discussed in Section **5**.

In Figure **1**, a slightly expanded region of that shown in Figure 11 of (Bennett, 2023), the electric field signals observed by the EMFISIS instruments on the Van Allen Probe (VAP) satellite at 2.5°S 154.6°W altitude 239 km from a single lightning flash located at 9.2°N 84.8°W, comprising four strokes, are shown. In Figures **1b**, **1d** and **1f**, the temporal variations of the electric field components E_u, E_v and E_w along the three axes, U, V and W of the spinning VAP satellite are shown. The W axis is spin aligned and approximately vertical here. Figures **1a**, **1c** and **1e** display scalograms for the three electric field components computed using a continuous wavelet transform (CWT) as described in (Bennett, 2023). Scalograms display the time dependence of the frequency components of a waveform and feature higher temporal resolution at higher frequencies following the cone of influence (COI) function. An example of the COI function centered at the time of the second pulse is shown in Figure **1e** by the white curved dashed line. An impulsive disturbance at a single time sample in the electric field would produce a scalogram peak with the shape of the COI. The COI also indicates how data outside the time period used in the CWT may affect the scalograms. The COI of the boundary effects is shown as a curved black dashed line in **1a**, **1c** and **1d**. Scalogram values at frequencies below the boundary COI are unreliable. For example, in **1a** and **1c**, at the start of the time period, the greenish region below the COI is a boundary artifact.

The appearance times of the four peaks seen in Figure **1f**, are delayed by 20, 31, 30 and 7 ms as indicated above Figure **1e** relative to the arrival times of LG pulses at the subsatellite location. The curve shown in Figure **1g** is the sum of the waveforms from the Nickolaenko et al. (2004) model using parameters for the stroke intensities and arc distances from the subsatellite position to the stroke location detected by the World Wide Lightning Locator Network (WWLLN) over the time period shown. WWLLN is a global Very Low Frequency (VLF; 3-30kHz) lightning location system capable of finding the radiated energy, time and location of individual lighting strokes with ~10 km spatial accuracy, ~10 μs temporal accuracy and ~90% efficiency for high peak current strokes (Abarca et al., 2010; Holzworth et al., 2019; Hutchins et al., 2012; Jacobson et al., 2006; Rodger et al., 2006). Red vertical lines in Figures **1b**, **1d** and **1f** mark the three peaks in the composite model electric field function shown in Figure **1g**. The (Nickolaenko et al., 2004) model propagation speed of 245 km/s accurately matches the observed travel speed 245±5 km/s for ELF pulses observed at ground level by the World ELF Radiolocation Array (WERA), as discussed by (Bennett, 2023) and shown in Figure 10 of that article. The propagation speed of LG pulses through the Earth Ionosphere waveguide (EIWG) is primarily a function of the altitude of the EIWG upper boundary (EIWGUB) as discussed in (Golkowski et al., 2018). All of the VAP data in this article were acquired near local midnight, so that most of the stronger LG pulses travelled entirely through regions with higher EIWGUB altitudes. The second of the four pulses seen in Figure **1f** was detected in the Geostationary Lightning Mapper (GLM) (Bateman et al., 2020; Goodman et al., 2013; Rudlosky et al., 2019) data, but not in the WWLLN data.

A feature of the data shown in Figure **1c** that was not noticed by (Bennett, 2023) is the presence of two "Precursor" streaks most clearly seen in the E_v scalograms near 10 kHz. These precursors first appear approximately 4 ms after the red vertical lines in Figure **1a**-**1f**. A similar precursor is only marginally apparent preceding the fourth peak and no significant precursor appears before the second pulse in Figure **1f**. Examination of other VAP data bursts reveals that such precursors often do appear, albeit only in a minority of the cases for which clear, well identified LG peaks are seen in the scalograms. In numerous other cases, such precursors are found very well correlated with the subsatellite arrival time of EMPs predicted using the Nickolaenko et al. (2004) model and WWLLN measured times and locations. In the first nine figures in the Supplemental materials **S1**, 22 distinct examples of precursors may be seen.

Another significant example involving multiple strokes from a single lightning flash is shown in Figure **2**. In this case, a single flash at 12.7°N 152.8°E comprising three WWLLN strokes occurring in rapid succession produces three precursors and three bipolar pulses in the electric field components. The bipolar pulses are narrowest in the E_v component and broadest in the E_u component. The precursors in this case appear strongest in the E_u component, are significant in the E_v component but lost in the noise in the E_w component. The relatively broad temporal extent of the precursors suggests that they may be a novel form of spread F, but seen at frequencies far below radar frequency and in terms of direct propagation delay rather than as reflected pulses. Validation of the assumed 245 km/s group velocity for propagation through the EIWG in this case is validated by the WERA data for these LG pulses shown in the last three figures in the Supplemental materials.

Despite the substantial propagation delays for the LG events seen in Figures **1f** and **2d**, no significant increase in the widths of the pulses (relative to the model pulses in Figures **1g** and **2g**) from the propagation through the EIWG from the location of the lightning flash to the subsatellite point was seen. This dispersionless propagation of LG EMPs through the lower ionosphere exemplified by Figures **1** & **2** is in stark contrast to the characteristics of normal whistlers. In the following section **3**, the detailed behavior of normal whistlers is quantitatively described. In section **4**, unusual dispersion events are discussed. A possible physical explanation of both the “spread F like” precursors and the delayed bipolar dispersionless pulses will be discussed in Section **5**.

3 Wave Vector Analysis for Normal Whistler Events

3.1 Normal Two Fluid Plasma Dispersion Relations

In (Bennett, 2023) it was empirically found, for propagation angles θ relative to the local magnetic field not close to ±90°, that both the phase and group velocities versus frequency of fast magnetosonic “whistler” waves for frequencies above the relevant ion cyclotron frequency and below the electron cyclotron frequency have a square root dependence on frequency insensitive to ion mass. Numerically the group velocity vs. frequency is approximately

$$V_{group} = 189\,\frac{km}{s\sqrt{Hz}}\sqrt{\frac{75\,mm^{-3}}{N_e}\frac{B}{31\,\mu T}}\sqrt{f}\ , \qquad (1)$$

while the phase velocity is approximately

$$V_{phase} = 112\ \frac{km}{s\sqrt{Hz}} \sqrt{\frac{75\ mm^{-3}}{N_e}\frac{B}{31\ \mu T}}\ \sqrt{f cos(\theta)}\ . \tag{2}$$

These general and characteristic features of the classical whistler portion of the dispersion relations (De Jonghe & Keppens, 2021b) are seen in observational data for whistlers in "normal" plasma regions, but are *violated* in regions of unusual dispersion.

3.2 Normal Dispersion Relation Observations

Figure **3** of the present work shows the scalograms from a 1.6 second portion of the scalograms shown in Figure **5** of (Bennett, 2023). The overall travel time, including the propagation time through the EIWG to the subsatellite location, ΔT_0, followed by the passage upwards through the ionosphere to the satellite detectors is given by the integral of the inverse group velocity over the path length as

$$\Delta T = \int \frac{ds}{V_{group}(s)} = \Delta T_0 + DC/\sqrt{f}\ . \tag{3}$$

In the equality on the right hand side of expression (3), the dispersion constant (DC) value implicitly represents the integral over all variations along the path *through the ionosphere* of the factors in expression (1). Superimposed over the scalograms in Figure **3**, the white vertical dashed line shows the arrival time of an LG pulse at a time ΔT_0 after the WWLLN observed stroke time. The three curved red dashed lines show three dispersion curves having DC values of 0.1, 12 and 24 $s\sqrt{Hz}$, and having the same arrival time at the subsatellite location as the white dispersionless case. For DC values much less than 0.1 $s\sqrt{Hz}$, *normal* whistlers appear effectively dispersionless, arriving at a time ΔT_0 after the associated lightning stroke.

3.3 Wavevector Analysis of Normal Dispersion Observations

Figure **4** of the present work shows a wave vector analysis using the amplitudes along the four superimposed dispersion curves indicated by dashed lines in Figure **3**. At each frequency and time along the dispersion curves having DC values indicated in the column titles for Figures **4a**, **4f**, **4k** and **4p**, the complex amplitudes of the scalograms for the electric and magnetic fields are used to compute the Poynting vector

$$\boldsymbol{S}(f) = \boldsymbol{E}(f) \times \boldsymbol{B}^*(f)\ \ , \tag{4}$$

and the unit Poynting vector

$$\widehat{\boldsymbol{S}}(f) = \boldsymbol{S}(f)\ /\ |\boldsymbol{S}(f)|\ \ . \tag{5}$$

The absolute values of the scalar product of the unit Poynting vector with each of the unit vectors in the mean field aligned (MFA) coordinate system described in (Min et al., 2017; Ritter et al., 2013) as a fuction of frequency are shown in the top three rows of Figure **4**. The MFA coordinate labels here (μ, ϕ, and ν) follow the notation of Min et al. (2017). The scalar products along the local magnetic field are indicated by $|S\bullet\mu|$ in the ordinate label in **4a**. The scalar products along the magnetic East direction in the horizontal plane are indicated by $|S\bullet\phi|$ in the ordinate label in **4c**. The scalar products along the direction orthogonal to the first two directions, approximately vertical in the equatorial region, are indicated by $|S\bullet\nu|$ in the ordinate label in **4b**. In **4d**, **4i**, **4n** and **4s**, the absolute value of the electric and magnetic field scalogram components are shown as a function of frequency. The random phase approximation (RPA) for the phase velocity as a function of frequency is computed according to the method described by (Bennett, 2023) from the complex scalogram amplitudes along each of the four dispersion curves shown in Figure **3**, and is plotted in Figure **4e, 4j, 4o** and **4t**.

Expression 2 is used to estimate the propagation angles θ in Figure **4e, 4j, 4o** and **4t** by fitting the high frequency behavior of the four cases. These estimated angles are shown in blue in the last row of Figure **4** and the phase velocity vs. frequency variation of expression 2 is shown by the green line in Figure **4e, 4j, 4o** and **4t** above the oxygen cyclotron frequency. Below the oxygen cyclotron frequency the phase velocity is shown by the horizontal section of the green line at its long wavelength limit assuming the plasma is predominantly O^+ ions.

Since the "noise" of other contributions to the scalogram amplitudes along the four dispersion curves is not negligible, significant fluctuations are seen in the estimated Poynting vector projections displayed in the top three rows of Figure **4**. Even so, it seems the direction of the *energy* flow for the low dispersion whistler and its echos are traveling in approximately consistent directions, in contrast to the apparent variation in the direction of the *wavevector* suggested in the last row of Figure **4**. The sign of the energy propagation direction is irrelevant in the plots of the absolute values of the energy propagation direction cosines shown in the top three rows of Figure **4**. This whistler and its echos are travelling obliquely in the MFA coordinate system, with unit Poynting vector projections of approximately 0.8, 0.5 and 0.4 along the μ (magnetic field B), ν (~vertical), and ϕ (magnetic East) directions.

Even though the dispersion constant (DC) values are dramatically different for the four cases displayed in Figure **4**, the RPA estimated phase velocities for all four cases are not so different, and are consistent with slightly different $\cos(\theta)$ angular factors. The reason for the great differences between the DC values is that they represent integrated totals of the dispersion over the full distance (in the last two cases including the echoing path) from source to detector. This sensitivity of the DC values to the integrated dispersion along the full path from source to detection was extensively exploited and discussed in (Bennett, 2023). In contrast, the four dispersiveness coefficients (50, 50, 80 & 112) in the legends in **4e**, **4j**, **4o** and **4t** are local measurements, characteristic of the conditions of the ionosphere at the location of the detectors, rather than an integral measure along the full propagation path.

Finally, some measure of the fidelity of the RPA estimates for phase velocity can be judged by the degree to which the scalograms are found to have significant values above the ambient “noise”. For example, for the Bu component displayed in **3a**, scalogram amplitudes for frequencies below 100 Hz appear to decrease to the level of the “background” amplitudes primarily associated with the population of slow magnetosonic waves discussed in (Bennett, 2023). Other components are similarly “lost” in the background noise at a variety of frequency levels. As a guide for the interpretation of which frequencies have meaningful values for both the direction projections shown in the top three rows, and the phase velocities shown in the bottom row of Figure **4**, the cyclotron frequencies for Oxygen and Hydrogen are shown by the white and magenta dashed lines in Figure **3** and cyan and magenta dashed lines in Figure **4** in order to more readily identify regions having significant amplitudes for all six electromagnetic components.

4 Wave Vector Analysis for Unusual Disperion Events

4.1 A Region of Unusual Dispersion

Figure **5** of the present work shows the scalograms from a single data burst acquired shortly before the burst scalograms shown in Figure 9 of (Bennett, 2023). In this figure, the arrival times of EMPs from every lightning strike detected by the WWLLN are shown by the vertical dashed white lines. Not a single normally dispersed whistler is observed during this data burst. This data has the character described in (Bennett, 2023) for periods that the Van Allen probe is passing through the root of a plasma bubble contiguously connected to the EIWG. Specifically,

1. the dispersion constant (DC) values become anamolously small relative to the estimate from the international reference ionosphere (IRI) model for the time and location of the satellite,
2. it is observed that the “spikes” in the scalograms corresponding to anamolously small DC values do not extend much above 1 kHz, in contrast to normal, very low dispersion cases outside plasma bubble regions that extend all the way to the Nyquist frequency as seen in Figure **3**,
3. the electric field fluctuations become enhanced by several orders of magnitude relative to typical values seen just before or just after entering the bubble region,
4. the magnetic field fluctuations are not especially enhanced relative to typical values outside the bubble region,
5. where both electric and magnetic field fluctuations are significant relative to their surroundings, the estimated phase velocity is orders of magnitude faster than expected relative to the IRI model estimate.

The last three of these points are clearly seen in the spectra, as shown by comparison of the fourth column relative to the first or third columns in Figure 7 of Bennett (2023).

In the first portion of the data shown in Figure **5** prior to the identified “Period of Interest”, there are a great number of dispersionless spikes seen in the electric field scalograms, most of which do not have corresponding well isolated spikes substantially above the ambient clutter noise from the ubiquitous slow magnetosonic waves (Bennett, 2023) in the magnetic field scalograms, so that a wavevector analysis of the sort described for Figure **4** is not feasible because of the high degree of “clutter noise”. The number of spikes is much greater than the number of detected WWLLN strokes during this period. Furthermore, the timing of the WWLLN stroke arrivals do not line up well with the strong dispersionless spikes in the VAP data. Since the wavevector analysis shown above in Figure **4** relies on having scalogram amplitudes for all six electric and magnetic field components that are reasonably stronger than the surrounding "noise" of other waves, the region indicated by the bracket with arrows labeled "Period of Interest" has been chosen for further wavevector analysis because of the availability of significant dispersionless spikes in the magnetic field scalograms. This region is also of interest as it appears to be at the edge of a plasma bubble, since the dispersionless spikes are suddenly not seen after this period.

4.2 Scalograms from A Region of Unusual Dispersion and the Cone of Influence

Figure **6** shows in more detail scalograms of the three magnetic and electric field components for the bracketed region indicated in Figure **5**. Superposed on the scalograms are eight white vertical dashed lines labeled #1 - #8 chosen to pass through peaks in either the magnetic or electric scalograms. The four dashed red vertical lines are drawn at the predicted arrival times of LG waves at the subsatellite location, using the WWLLN measured locations and strike times assuming a propagation speed through the EIWG of 245 km/s. For each of the four WWLLN detected waves, the angular distance from the subsatellite point to the WWLLN determined strike location is indicated in **6f** by the blue text numbers.

The noisiness of the following wavevector analysis for propagation direction and phase velocity may be attributed to the variability in the contributions from the numerous other waves present at the times chosen for analysis. The cone of influence (COI) shown by the curved red dashed lines superimposed over the scalogram plots in Figure **6** shows the boundary COI, as described in section 2 above. The COI also represents the "confusion time range" over which other waves contribute to the scalogram amplitudes associated with a given peak. For example, the strongest spike in the electric field scalograms, labeled #6, spreads more broadly in time at lower frequencies just as does the COI shown by the curved white dashed line in **6d**, **6e** and **6f** centered at peak #6.

4.8 Foamy Behavior of Unusual Dispersion Regions

The wavevector analysis shown in Figure **7** for cases labeled #3, #4, #5 and #8 in Figure **6** displays an unusual phase velocity distribution. At frequencies below the local oxygen cyclotron frequency, the RPA estimated phase velocity is approximately 30 Mm/s for all four cases. For cases #3 and #5, above the oxygen cyclotron frequency the RPA phase velocity drops to approximately 2 Mm/s and *is approximately constant*. In contrast, cases #4 and #8 in the 2^{nd} and 4^{th} columns, appear to alternate between 2 Mm/s and 30 Mm/s regions.

The results displayed in Figures **7e** and **7o** are in stark contrast to the normal variation of phase velocity as a function of frequency seen in Figures **4e**, **4j**, **4o** and **4t**. In the Figure **7e** and **7o** plots the constancy of the phase velocity above the relevant local cyclotron frequency, Oxygen in this case, cannot be explained by any normal IRI model. In general, the local plasma dispersiveness produces a phase velocity increasing as the square root of the frequency, as in expression **2**. Evidence that the phase velocity for these waves is not merely locally dispersionless, but also nearly dispersionless along their full path through the ionosphere to the satellite is simply that the appearance in the scalograms such as in Figures **1** or **2** is of purely vertical spikes with negligible indication of dispersion beyond the Nickolaenko et al. (2004) model, *despite substantial overall propagation delays*.

The ionospheric length of the propagation path followed by LG waves cannot be less than a purely vertical path of approximately 190 km from the EIWGUB to the satellite, and thus the propagation delays of 12 and 25 ms for events #1 & #2 as indicated in Figure **6a**, correspond to mean speeds no less than 16 and 8 Mm/s. Although the magnetic field scalogram spikes in Figure **6a**, **6b** & **6c** for events #1 & #2 have such high “clutter noise” that a wavevector analysis of the type shown in figure **7** is unreliable, these speeds at least do have the same order of magnitude as the RPA estimates shown in the last row of plots in Figure **7** for peaks #3, #4, #5 and #8.

5 Propagation of Magnetohydrodynamic Waves Through A Model Plasma Foam

Even in the absence of magnetic fields or ionization, the propagation of acoustic waves through foamy mixtures of gaseous and liquid phases is complex, as discussed for example in (Benjelloun & Ghidaglia, 2021; Elias et al., 2020; Pierre et al., 2013). Remarkably, prior to experimental confirmation, in 1941 Wood, on the basis of physical arguments, argued that the speed of sound in a mixture of two fluids would be that of a single fluid having density equal to the volumetric mean density of the two fluids, and compressibility equal to the volumetric mean compressibility. In a mixture of air bubbles in water for example, the speed of sound, according to Wood’s law, may be orders of magnitude slower than the speed of sound in either water or air. This is because the mixture density is dominated by the water fraction, while the mixture compressibility is dominated by the air fraction. It has been found (Elias et al., 2020) that Wood’s law indeed reliably predicts the velocity of sound in most liquid foams *when the bubbles are much smaller than the acoustic wavelength*.

Isolated small air bubbles in water are most likely to be nearly spherical. By contrast, low density plasma bubbles embedded in higher density plasma at the bottom of the ionosphere are expected to extend along local magnetic field lines. In the model of a small region of the lower ionosphere illustrated in Figure **8**, “normal” plasma is represented by the gold colored material while very low plasma density depletion bubbles are represented by voids. In this model, the bubbles are drawn with circular shapes in the plane perpendicular to **B**, and with a random assortment of positions and diameters. The presence of the magnetic field produces a sensitive dependence on the direction of propagation of magnetohydrodynamic (MHD) waves relative to **B**. With the local speed of sound much less than the Alfven speed, magnetosonic waves tend to separate into fast waves moving nearly perpendicular to **B** and slow waves moving nearly parallel to **B** (Jackson, 1975). As the waves discussed here are fast, I consider waves moving exactly perpendicular to **B**. Such waves propagate with a speed dependant on the sum of hydrostatic and magnetic pressures.

In the plane perpendicular to B, the section of “foamy” plasma shown has dimensions of a single wavelength in both the East/West and Up/Down directions. With the approximation that the compressibility of normal density plasma is much less than the compressibility of low density bubbles, the speed of fast magnetosonic waves in the mixture becomes much less than the speed in either normal density plasma or low density bubbles. This speed is also a sensitive function of the bubble volumetric fraction, and may vary erratically from one sample to the next. The wide variety of propagation delays seen in Figures **1** and **2** can be explained by this erratic variation.

For wavelengths shorter than the smallest of the plasma bubble radii in this model, MHD waves would tend to propagate only within the circular cross section “waveguides” bounded by the high conductivity plasma “walls”, as either (Jackson, 1975) transverse electric or transverse magnetic modes. With a variety of bubble diameters and plasma densities within the bubbles, the group velocities of short wavelength modes passing through these waveguides would also be variable. The spread in the arrival times of high frequency, short wavelength waves seen in the form of “precursors” in Figures **1** and **2** can be explained by this process. Because of the low plasma density within these effective waveguides, the highest propagation speed may be quite high, and the earliest precursor signals may appear immediately after the arrival of LG pulses at the subsatellite location, as seen in the numerous examples in Figures **1** and **2** and the supplemental figures.

Finally, the frequency spread of the “precursors” is sometimes limited to a narrow range (e.g. from just below to just above 10 kHz in the Figure **1c** case), but more often extends over a wider frequency range (e.g. from about 1 kHz to 20 kHz in the Figure **2a** case). Examination of the various examples of “precursors” in the first nine supplemental figures reveals that the frequency spread of the “precursors” is relatively consistent over the brief periods shown in these figures. Examination of the numerous examples shown in Figures **1** and **2** and the supplemental figures further reveals that the unusual, nearly dispersionless spikes in the scalograms do not usually extend much above a few kHz. From the disperion relations for fast magnetosonic waves travelling in a primarily O^+ plasma, as shown in Figure **1d** of Bennett (2023), this frequency corresponds to wavelengths of a few km. Both the lower frequency limit of the extent of the “precursors” and the upper frequency limit of the scalogram spikes suggest that the mean spacing of the bubbles in Figure **8** is typically on the order of magnitude of 1 km. This model then naturally explains the lower frequency bound of the “precursors” and the upper frequency bound on the dispersionless scalogram spikes.

6 Discussion and Conclusions

Another characteristic of “foamy” behavior is strong attenuation. This effect is more difficult to prove directly with the Van Allen probe observations. In some rare cases, such as those displayed in Figures **1** and **2**, multiple intense strokes of lightning are seen emerging from a single location that may be identified with individual LG pulses measured by the Van Allen probe detectors. With nearly identical paths traversed from source to detector, the correlation between propagation delay and attenuation may be made. However, because of the inherent variability in foamy plasma model illustrated in Figure **8**, the uncertainties in these measurements within a single burst of data are quite large. For the data shown in Figure **1**, it is found that an attenuation of 49±22% corresponds to a propagation delay of 19±12 ms, while for the data shown in Figure **2**, an attenuation of 1±0.7% corresponds to a propagation delay of 131±5 ms. These values plotted in Figure **9** provide suggestive evidence for strong attenuation of fast magnetosonic waves with propagation distance through foamy plasma. A more indirect manifestation of the strong attenuation of LG waves passing through such hypothetical foamy plasma is the fact that most lightning strokes do not produce detectable whistler events in the Van Allen probe data.

In (Zheng et al., 2015) a search for coincident detections of LG events by the Van Allen probe satellites and the WWLLN was made. For the subset of lightning strikes within 18° of the subsatellite location, only 15.3% of the strikes were detected by the Van Allen probe instruments. The relatively low 15% coincidence rate found in this study could be explained by the presence of underlying plasma bubble foam covering approximately 85% of the bottom of the ionosphere. In (Jacobson et al., 2018) it was found that most lightning strokes were not detected by the C/NOFS instruments, while occasionally there was greatly enhanced transmission of LG waves to the satellite. Quantitatively, from line 6 of table 1 of (Jacobson et al., 2018) listing a population of 136-thousand WWLLN strokes having predicted strong Poynting vector fluence at the subsatellite point, the estimated number of coincident Vector Electric Field Investigation (VEFI) whistlers, from line 13 of table 1 was only 19-thousand (14%). These authors suggested that km-scale D-layer irregularities might be responsible for these effects. Frequently appearing foamy plasma bubble roots of the sort discussed here in connection with Figure **8** could explain both the lack of detection for most lightning strokes noted by (Jacobson et al., 2018) and the occasional greatly enhanced transmission. The rare enhanced transmission observations would correspond to cases for which the C/NOFS satellite was either immersed in, or just above, a plasma bubble root, while the more common lack of detection would correspond to foamy, strongly attenuating bubbles not extending up to the C/NOFS satellite that effectively absorbed most of the LG energy. Despite the quite different analysis approaches of (Zheng et al., 2015) and (Jacobson et al., 2018), their coincident rates between satellite observations of whistlers and WWLLN detected lightning strokes are in reasonable agreement.

In conclusion, it is suggested that most (~80%) of the bottom of the nocturnal equatorial ionosphere is covered with a "foamy" layer of plasma bubbles that extend contiguously down to neutral atmosphere. Whether this foam is turbulent is an open question. The detailed spatial structure of this foam is an open question. The possibility of two-phase foamy structure at the base of the ionosphere may complicate theoretical analyses that implicitly assume a single-phase medium. Many other such questions remain open, but it is hoped that follow up observations and theoretical analysis might be stimulated by the present suggestions.

Acknowledgments

This work is entirely self funded by the author. WWLLN data was purchased from the University of Washington (https://wwlln.net). Van Allen Probe wave data used in this paper may be downloaded at no cost as described in the following paragraph, and the work of the EMFISIS team in its production is gratefully acknowledged. WERA data used in the preparation of this paper was provided by Jerzy Kubisz of the Astronomical Observatory of the Jagiellonian University, and the author thanks him and the WERA project personnel for their help in understanding this data.

Open Research

Van Allen Probe data used in this paper can be found in the EMFISIS archive (http://emfisis.physics.uiowa.edu/data/index). In this index file, descriptions of each of the relevant data sets, including the file naming format, are provided. The specific level 2 data products involved in the present work include the "WFR-waveform-continuous-burst_emfisis-

L2", "WFR-spectral-matrix-diagonal_emfisis-L2", "magnetometer_uvw_emfisis-L2". The specific level 3 data products are "magnetometer_hires-geo_emfisis-L3". Swarm data used in this paper is provided by the European Space Agency and can be accessed online at https://swarm-diss.eo.esa.int. The high rate VFM data was taken from the level 1b "latest_baselines" folder containing "MACx_HR" files for each of the three Swarm satellites. WERA data used in this paper is described in detail on the WERA project website: http://www.oa.uj.edu.pl/elf/index/projects3.htm and may be freely available for scientific analysis by contacting the WERA personnel. WWLLN data was purchased from the University of Washington (https://wwlln.net). GLM data is available at no cost from the Geostationary Operational Environmental Satellites-R Series web site (https://www.goes-r.gov), but the user must register to obtain the GOES-R Series GLM L2+ Data Product "GRGLMPROD" and must select an appropriate time range for data access on the web-page: https://www.avl.class.noaa.gov/saa/products/search?datatype_family=GRGLMPROD.

References

Abarca, S.F., Corbosiero, K.L., & Galarneau, T.J. Jr. (2010). An evaluation of the Worldwide Lightning Location Network (WWLLN) using the National Lightning Detection Network (NLDN) as ground truth. *Journal of Geophysical Research, 15*, D18206, doi:10.1029/2009JD013411

Abdu, M.A., Batista, I.S., Reinisch, B.W., MacDougall, J.W., Kherani, E.A., & Sobral, H.H.A (2012). Equatorial range spread F echoes from coherent backscatter, and irregularity growth processes, from conjugate point digital ionograms., *Radio Science*, 47, RS6003, doi:10.1029/2012RS005002

Akhtar, N, Hussain, S., & Mahmood, S. (2021). Nonlinear propagation of fast and slow magnetosonic waves in collisional plasmas. *Contributions to Plasma Physics*. https://doi.org/10.1002/ctpp.202000210

Balan, N., Liu, LiBo & Le, H. (2018). A brief review of equatorial ionization anomaly and ionospheric irregularities. *Earth and Planetary Physics, 2*, 257-275, https://doi.org/10.26464/epp2018025

Bateman, M., Mach, D., & Stock, M. (2020). Further investigation into detection efficiency and false alarm rate for the geostationary lightning mappers aboard GOES-16 and GOES-17. *Earth and Space Science, 8*, 2020EA001237. https://doi.org/2020EA001237

Benjelloun, S. & Ghidaglia, J.-M. (2021). On the sound speed in two-fluid mixtures and the implications for CFD model validation. European Journal of Mechanics / B Fluids, 90, 152-168. https://doi.org/10.1016/j.euromechflu.2021.09.002

Bennett, C.L. (2023). A Novel Population of Slow Magnetosonic Waves and a Method for the Observation of the Roots of Plasma Bubbles in the Lower Ionosphere. *ESS Open Archive*. January 17, 2023, doi:10.1002/essoar.10511954.3

Chou, M.Y., Yue, J., Sassi, F., Huba, J., McDonald, S.E., Tate, J.L., et al, (2022). Modeling the Day-to-Day Variability of Midnight Equatorial Plasma Bubbles with SAMI3/WACCM-X. Authorea. December 27, 2022, doi:10.22541/essoar.167214177.74303978/v1

De Jonghe, J. & Keppens, R. (2020a). A two-fluid analysis of waves in a warm ion-electron plasma. *Plys. Plasmas*. *27*, 122107, doi:10.1063/5.0029534

De Jonghe, J. & Keppens, R. (2020b). Two-Fluid Treatment of Whistling Behavior and the Warm Appleton-Hartree Extension. *Journal of Geophysical Research: Space Physics, 126,* e2020JA028953, doi:10.1029/2020JA028953

De Michelis, P., Consolini, G., Alberti, T., Tozzi, R., Giannattasio, F., Coco, I., et al. (2022). Magnetic Field and Electron Density Scaling Properties in the Equatorial Plasma Bubbles. *Remote Sens. 14*, 918, doi:10.3390/rs14040918

De Michelis, P., Consolini, G., Tozzi, R., Pignalberi, A., Pezzopane, M., Coco, I., et al. (2021). Ionospheric Turbulence and the Equatorial Plasma Density Irregularities: Scaling Features and RODI. *Remote Sens. 13*, 759, doi:10.3390/rs13040759

Elias, F., Crassous, J., Derec, C., Dollet, B., Drenckhan, W., Gay, C., et al. (2020). The Acoustics of Liquid Foams, *Current Opinion in Colloid & Interface Science, 50*, 10139, doi:10.1016/j.cocis.2020.101391

Golkowski, M., Sarker, S.R., Renick, C., Moore, R.C., Cohen, M.B., Kulak, A., Mlyanarczyk, J., & Kubisz, J. (2018). Ionospheric D Region Remote Sensing Using ELF Sferic Group Velocity. *Geophysical Research Letters, 45*, 12,739-12,748, doi:10.1029/2018GL080108

Goodman, S., Blakeslee, R., Koshak, W., Mach, D., Bailey, J., Buechler, D., et al. (2013). The goes-r Geostationary Lightning Mapper (GLM). *Atmospheric Research, 125-126*, 34-49, doi:10.1016/j.atmosres.2013.01.006

Goodman, S., Mach, D., Koshak, W., Blakeslee, R. (2012). Algorithm theoretical basis document: GLM lightning cluster-filter algorithm. Version 3.0. July 30, 2012. NOAA NESDIS Center for satellite applications research.

Heelis, R. (2004). Electrodynamics in the low and middle latitude ionosphere: A tutorial. *Journal of Atmospheric and Solar-Terrestrial Physics, 66*(10), 825-838, doi:10.1016/j.jastp.2004.01.034

Holzworth, R.H., McCarthy, M.P., Brundell, J.B., Jacobson, A.R. & Rodger, C.J. (2019). Global distribution of superbolts. *Journal of Geophysical Research: Atmospheres, 124*, 9996-10,005, doi:10.1029/2019JD030975

Huba, J.D. (2023). Resolution of the equatorial spread F problem: Revisited. *Front. Astron. Space Sci.* 9:1098083, doi:10.3389/fspas.2022.1098083

Hutchins, M.L., Holzworth, R.H., Rodger, C.J., & Brundell, J.B. (2012). Far-field power of lightning strokes as measured by the world-wide lightning location network. *Journal of Atmospheric and Oceanic Technology, 29*, 1102-1110. https://doi.org/10.1175/JTECH-D-11-00174.1

Hysell, D.L., Larsen, M.F., Swenson, C.M., Barjatya, A., Wheeler, T.F., Sarango, M.F., et al. (2005). Onset conditions for equatorial spread F determined during EQUIS II. *Geophysical Research Letters*, *32* (L24104), doi:10.1029/2005GL024743

Immel, T.J., Mende, S.B., Frey, H.U., Peticolas, L.M., & Sagawa, E. (2003). Determination of low latitude plasma drifts speeds from FUV images. *Geophysical Research Letters, 30*(18), 1945, doi:10.1029/2003GL017573

Jackson, J.D. (1975). *Classical Electrodynamics.* New York: John Wiley & Sons.

Jacobson, A.R., Holzworth, R.H., Pfaff, R. & Roderick H. (2018). Coordinated Satellite Observations of the Very Low Frequency Transmission Through the Ionospheric D Layer at Low Latitudes, Using Broadband Radio Emissions from Lightning. *Journal of Geophysical Research: Space Physics, 123*, 2926-2952, doi:10.1002/2017JA024942

Kelley, M.C., Makela, J.J., de La Beaujardiere, O., & Retterer, J. (2011). Convective Ionospheric Storms: A Review. *Rev. Geophys., 49*, RG2003, doi:10.1029/2010RG000340

Karan, D.K., Daniell, R.E., England, S.L., Martinis, C.R., Eastes, R.W., Burns, A.G., & McClintock, W.E. (2020). First zonal drift velocity measurement of equatorial plasma bubbles (EPBs) from a geostationary orbit using GOLD data. *Journal of Geophysics: Space Physics 125*, e2020JA028173, doi:10.1029/2020JA028173
Kil, H., Demajistre, R., & Paxton, L.J. (2004). F-region plasma distribution seen from TIMED/GUVI and its relation to the equatorial spread F activity. *Journal of Geophysical Research, 31*, L05810, doi:10.1029/2003GL018703
Kil, H., & Heelis, R.A. (1998). Global distribution of density irregularities in the equatorial ionosphere. *Journal of Geophysical Research, 103*, 407-417 doi:10.1029/97JA02698
Kil, H., Sun, K.A., Chang, H., Paxton, L.J., Nikoukar, R., & Lee, J. (2022). Characteristics and sources of electron density irregularities near and after midnight in the equatorial F region. Oral presentation SA55A-03 at AGU fall meeting, Chicago Illinois, USA. https://agu.confex.com/agu/fm22/meetingapp.cgi/Paper/1177560
Kudeki, E., & Bhattacharyya, S. (1999). Postsunset vortex in equatorial F-region plasma drifts and implications for bottomside spread F. *Journal of Geophysical Research*, 104(A12), 28, 163-28, 170, doi:10.1029/1998JA900111
Liang, J., Donovan, E., Jackel, B., Spanswick, E. & Gillies, M. (2016) On the 630 nm red-line pulsating aurora: Red-line Emission Geospace Observatory observations and model simulations. *Journal of Geophysical Research: Space Physics, 121*, 79880-8012, doi:10.1002/2016JA022901
Makela, J.J., & Kelley, M.C. (2003). Field-aligned 777.4-nm composite airglow images of equatorial plasma depletions. *Geophysical Research Letters, 30*(8), 1442, doi:10.1029/2003GL017106
Makela, J.J., Kelley, M.C., & Nicolls, M.J. (2006). Optical observations of the development of secondary instabilities on the eastern wall of an equatorial plasma bubble, *J. Geophys. Res., 111*, A09311, doi:10.1029/2006JA011646
Makela, J.J. & Miller, E.S. (2008). Optical observations of the growth and day-to-day variability of equatorial plasma bubbles, *J. Geophys. Res., 113*, A03307, doi:10.1029/2007JA012661
Makela, J.J. & Otsuka, Y. (2012). Overview of Nighttime Ionospheric Instabilities at Low- and Mid-Latitudes: Coupling Aspects Resulting in Structuring at the Mesoscale. *Space Sci. Rev 168*, 419-440, doi:10.1007/s11214-011-9816-6
Martinis, C., Eccles, J.V., Baumgardner, J., Manzano, J., & Mendillo, M. (2003). Latitude dependence of zonal plasma drifts obtained from dual-site airglow observations. *Journal of Geophysical Research, 108*(A3), 1129, doi:10.1029/2002JA009462
Mendillo, M., & Baumgardner, J. (1982). Airglow characteristics of equatorial plasma depletions. *Journal of Geophysical Research, 87*(A9), 7641-7652, doi:10.1029/JA087iA09p07641
Min, K., Takahashi, K., Ukhorskiy, A.Y., Manweiler, J.W., Spence, H.E., Singer, H.J., et al. (2017), Second harmonic poloidal waves observed by Van Allen Probes in the dusk-midnight sector. *J. Geophys. Res. Space Physics, 122*, 3013-3039, doi:10.1002/2016JA023770
Narayanan, V.L., Sau, S., Gurubaran, S., Shiokawa, K., Balan, N., & Emperumal, K. (2014). A statistical study of satellite traces and subsequent evolution of equatorial spread F based on ionosonde observations over dip equatorial site Tirunelveli, India. *Earth, Planets and Space*, 676(1), 160, doi:10.1186/s40623-014-0160-4

Nickolaenko, A.P., & Rabinowicz, L.M. (2004). Time domain presentation for ELF pusles with accelerated convergence. *Geophysical Research Letters, 31*, L05808, doi:10.1029/2003GL018700

Patra, A.K., Yokoyama, T., Yamamoto, M., Saito, S., Maruyama, T. & Fukao, S. (2005). Disruption of E region echoes observed by the EAR during the development phase of equatorial spread F: A manifestation of electrostatic field coupling. *Geophysical Research Letters, 32*(L17104), doi:10.29/2005GL022868

Pierre, J., Guillermic, R., Elias, R., Drenckhan, W., & Leroy, V. (2013). Acoustic characterization of liquid foams with an impedance tube. *The European Physical Journal E 36*(113), doi:10.1140/epje/i2013-13113-1

Piggott, W.R. & Rawer, K. (1972). URSI Handbook of Ionogram Interpretation and Reduction, second Edition, Novermber 1972, WDC A, Report UAG-23. https://repository.library.noaa.gov/view/noaa/10404

Pimenta, A.A., Bittencourt, J.A., Fagundes, P.R., Sahai, Y., Buriti, R.A., Takahashi, H., & Taylor, M.J. (2003). Ionospheric plasma bubble zonal drifts over the tropical region: A study using OI 630 nm emission all-sky images. *Journal of Atmospheric and Solar-Terrestrial Physics, 65*(10), 1117-1126, doi:10.1016/S1364-6826(03)00149-4

Ripoll, J.F., Farges, T., Malaspina, D.M., Lay, E.H., Cunningham, G.S., Hospodarsky, G.B. et al. (2020), Analysis of Electric and Magnetic Lightning-Generated Wave Amplitudes Measured by the Van Allen Probes. *Geophysical Research Letters, 47*, e2020GL087503, doi:10.1029/2020GL087503

Ritter, P., Luhr, H., & Rauberg, J. (2013), Determining field-aligned currents with the Swarm constellation mission. *Earth Planets Space, 65*, 1285-1294, doi:10.5047/eps.2013.09.006

Rodriguez-Zuluaga, J., Stolle, C., Yamazaki, Y., Xiong, C., & England, S.L. (2020). A synoptic-scale wavelike structure in the nighttime equatorial ionization anomaly. *Earth and Space Science, 8*, e2020EA001529, doi:10.1029/2020EA001529

Rudlosky, S., Goodman, S., Virts, K., & Bruning, E. (2019). Initial Geostationary Lightning Mapper observations. *Geophysical Research Letters, 46*, 1097-1104, doi:10.1029/2018GL081052

Santolik, O., Parrot, M., & Lefeuvre, F. (2003). Singular value decomposition methods for wave propagation analysis. *Radio Science, 38*(1), 1010, doi:10.1029/2000RS002523

Shiokawa, K., Otsuka, Y., Ogawa, T., & Wilkinson, P. (2004). Time evolution of high-altitude plasma bubbles imaged at geomagnetic conjugate points. *Annales Geophysicae, 29*(9), 3137-3143, doi:10.5194/angeo-22-3137-2004

Sivakandan, M., Mondal, S., Sarkhel, S., Chakrabarty, D., Sunil Krishna, M., V. Upadhayaya, A.K., et al. (2021). Evidence for the in-situ generation of plasma depletion structures over the transition region of geomagnetic low-mid latitude. *Journal of Geophysical Research: Space Physics, 126*, e2020JA028837, doi:10.1029/2020JA028837

Tsunoda, R.T. (1983). On the generation and growth of equatorial backscatter plumes: 2. Structuring of the west walls of upwellings. *Geophysical Research Letters, 88*(A6), 4869-4874, doi:10.1029/JA088iA06p04869

Wood, A.B. (1941). Textbook of Sound: Being an Account of the Physics of Vibrations with Special Reference to Recent Theoretical and Technical Developments, Second Edition, page 361, Macmillan Co., New York.

Woodman, R.F. (2009). Spread F - an old equatorial aeronomy problem finally resolved? *Ann. Geophysics 27*(5), 1915-1934, doi:10.5194/angeo-27-1915-2009

Woodman, R.F. and Hoz, C.L. Radar Observations of F Region Equatorial Irregularities. *Journal of Geophysical Research, 81*(31), 5447-5466, doi:10.1029/JA081i031p05447

Yokoyama, T., Yamamoto, M., Otsuka, Y., Nishioka, M., Tsugawa, T., Watanabe, S., & Pfaff, R.F. (2011). On postmidnight low-latitude ionospheric irregularities during solar minimum: 1. Equatorial Atmosphere Radar and GPS-TEC observations in Indonesia. *Journal of Geophysical Research, 116*, A11325, doi:10.1029/2011JA016797

Zheng, H., Holzworth, R.H., Brundell, J.B., Jacobson, A.R., Wygant, J.R., Hospodarsky, G.B., Mozer, F.S., & Bonnell, J. (2015). A statistical study of whistler waves observed by Van Allen Probes (RBSP) and lightning detected by WWLLN. *Journal of Geophysical Research: Space Physics, 121*, 2067-2079, doi:10.1002/2015JA022010

Figure 1. Scalograms (in **a**, **c**, and **e**) and time resolved plots (**b**, **d**, and **f**) of the electric field components are shown for a period while VAP-A passes through the root of a plasma bubble. In (**g**) the summation of the radial electric field contributions from all WWLLN detected lightning strokes within this time interval using the (Nickolaenko et al., 2004) model with WWLLN determined amplitudes is plotted. The percentage values shown above the three peaks in **f** represent the ratios of the observed peak amplitudes to the model amplitudes of the corresponding peaks seen in (**g**). The predicted arrival times at the subsatellite location using WWLLN/GLM stroke times are shown by the red/white dashed vertical lines in (**a**, **c** and **e**). The GLM times appear systematically later by 2 ms than the WWLLN times. The second of the peaks in (**f**) was seen by GLM but not detected by WWLLN. In the scalograms, some extraneous radio frequency interference at approximately 2 kHz and harmonics can be seen. The geographic location of the subsatellite point at the start of this data burst is shown in the title. Also shown is the location of the flash responsible for the four peaks in (**f**). The angular difference between these locations along the great circle is shown as $\Delta\theta$.

Figure 2. Scalograms and time resolved plots of VAP-A data with the same layout as in the previous figure are shown for a different period. The percentage values shown above the three peaks in (**f**) represent the ratios of the observed peak amplitudes to the model amplitudes of the corresponding peaks seen in (**g**). As in the previous figure, and in similar subsequent figures, the angular distance along the great circle containing both the satellite location and the relevant lightning flash location is indicated by the value of $\Delta\theta$ in the figure title.

Figure 3. Scalograms of the three magnetic and electric field components in the spinning U,V, W reference frame are displayed for a 1.6 s sample of EMFISIS data. The dashed line curves represent four distinct dispersion constant (DC) values that track the dispersed waves from a single lighting stroke detected by the WWLLN. In (**a**, **b** and **c**), scalograms for the Bu, Bv and Bw components of the magnetic field are shown. In **d**, **e** and **f**, scalograms for the Eu, Ev and Ew components of the electric field are shown. The approximate location and local solar time (LST) of the satellite at the time of this data collection is shown in the figure title.

Figure 4. The direction and speed for four different DC values are displayed for points along each of the dispersion curves shown in the previous figure. In (**a**, **f**, **k** and **p**), the absolute values for the projections of the Poynting unit vector **S** along μ (the direction of the local magnetic field **B**) are plotted as a function of frequency. Similarly in (**b**, **g**, **l** and **q**), projections along the ν direction (approximately vertical) of the MFA coordinate system are shown. Also similarly in (**c**, **h**, **m** and **r**), projections along the ϕ direction (magnetic East) of the MFA coordinate system are shown. In (**d**, **i**, **n**, **s**), the magnitudes of the electric and magnetic field amplitudes are shown as a function of frequency. In (**e**, **j**, **o**, and **t**) the RPA estimated phase velocities are plotted as a function of frequency.

Figure 5. Scalograms of the three magnetic and electric field components in the spinning U,V, W reference frame are displayed for a single burst of EMFISIS data. The white dashed vertical lines are plotted at the times of the arrival at the subsatellite location for every WWLLN event detected during this data burst. In (**a**, **b** and **c**), scalograms for the Bu, Bv and Bw components of the magnetic field are shown. In (**d**, **e** and **f**), scalograms for the Eu, Ev and Ew components of the electric field are shown. In (**g**), the satellite spin vector coordinates λ (in the fashion of latitude) and δ (in the fashion of longitude), characterizing the spin vector orientation relative to the local magnetic field, are indicated over the course of this data burst. The approximate location and local solar time (LST) of the satellite at the start of this data burst is shown in the legend for section (**g**).

Figure 6. Scalograms for the indicated subset of the time range in the previous figure are shown here. In (**a**, **b** and **c**), scalograms of the three magnetic field components are shown. In (**d**, **e** and **f**), scalograms of the three electric field components are shown. In (**f**), the arc distances, (80°, 18°, 162° and 79°), along the great circle containing the subsatellite location and the four WWLLN stroke locations are shown in blue text labels near the four dashed red vertical lines for the estimated arrival times at the subsatellite location of the four WWLLN strokes. The first two strokes appear sufficiently isolated that they may be tentatively identified with the scalogram spikes labelled #1 and #2 in (**f**).

Figure 7. A wavevector analysis with the same layout as that displayed in Figure **4** is shown here for the four times indicated in Figure (**6f**) by white vertical dashed lines and numbered #3, #4, #5 and #8. The locally dispersionless nature of the scalogram peaks seen in Figure 6 is validated by the nearly constant phase velocity values above the local Oxygen cyclotron frequency seen especially clearly in (**e** and **o**).

Figure 8. A physical model of a region of "foamy plasma" near the bottom of the ionosphere is illustrated. A sketch of the "Wood's law" derivation of the estimated speed of sound in the two-phase mixture is shown.

Figure 9. The variation of dispersionless pulse attenuation as a function of propagation delay through foamy plasma is plotted. The two points with error bars shown represent the two cases displayed in Figures **1** and **2** above.

Figure 1.

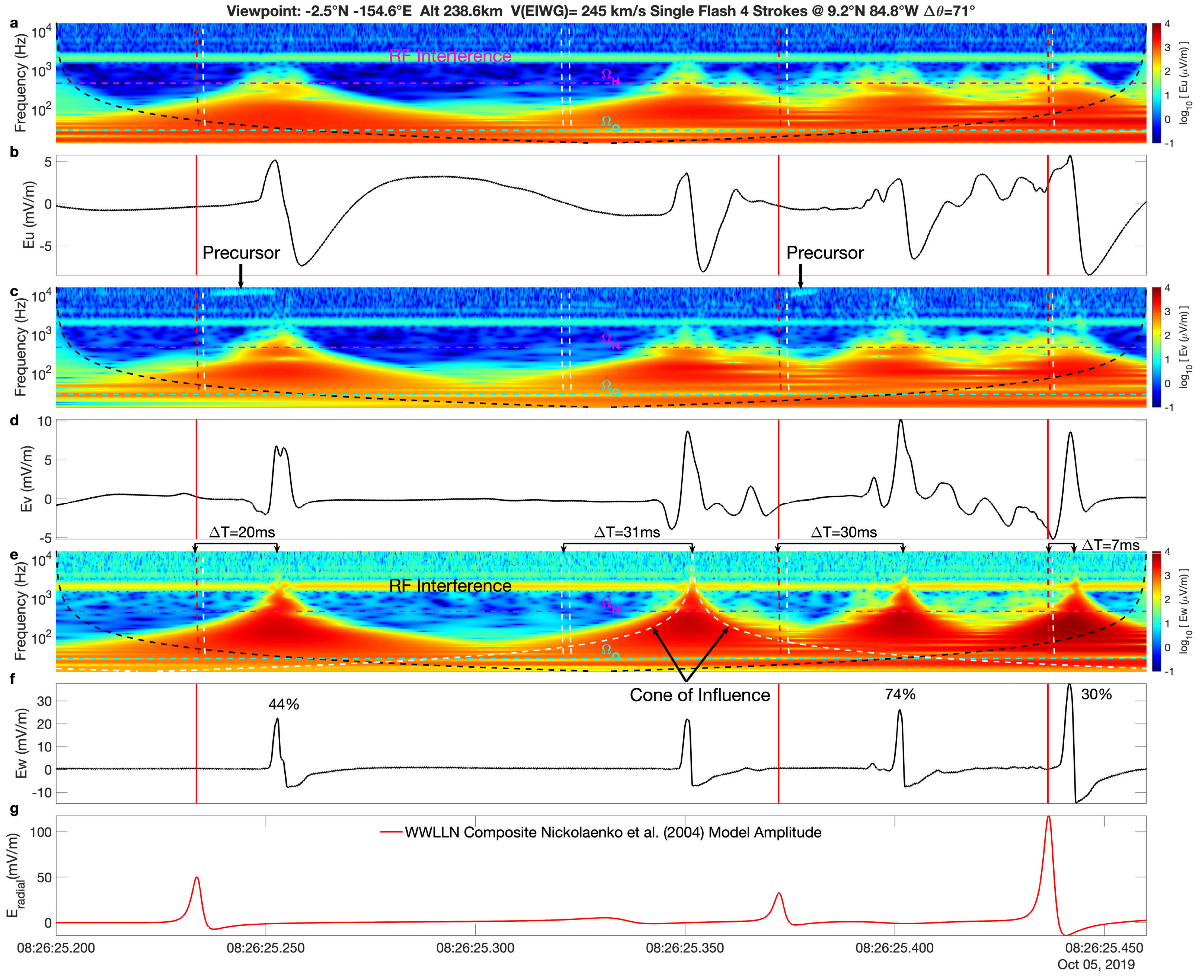

Viewpoint: -2.5°N -154.6°E Alt 238.6km V(EIWG)= 245 km/s Single Flash 4 Strokes @ 9.2°N 84.8°W Δθ=71°
a
b
c
d
e
f
g
Frequency (Hz)
RF Interference
Eu (mV/m)
Precursor
Precursor
Ev (mV/m)
ΔT=20ms
ΔT=31ms
ΔT=30ms
ΔT=7ms
Cone of Influence
Ew (mV/m)
44%
74%
30%
WWLLN Composite Nickolaenko et al. (2004) Model Amplitude
E_radial(mV/m)
log10 [Eu (μV/m)]
log10 [Ev (μV/m)]
log10 [Ew (μV/m)]
08:26:25.200
08:26:25.250
08:26:25.300
08:26:25.350
08:26:25.400
08:26:25.450
Oct 05, 2019

Figure 2.

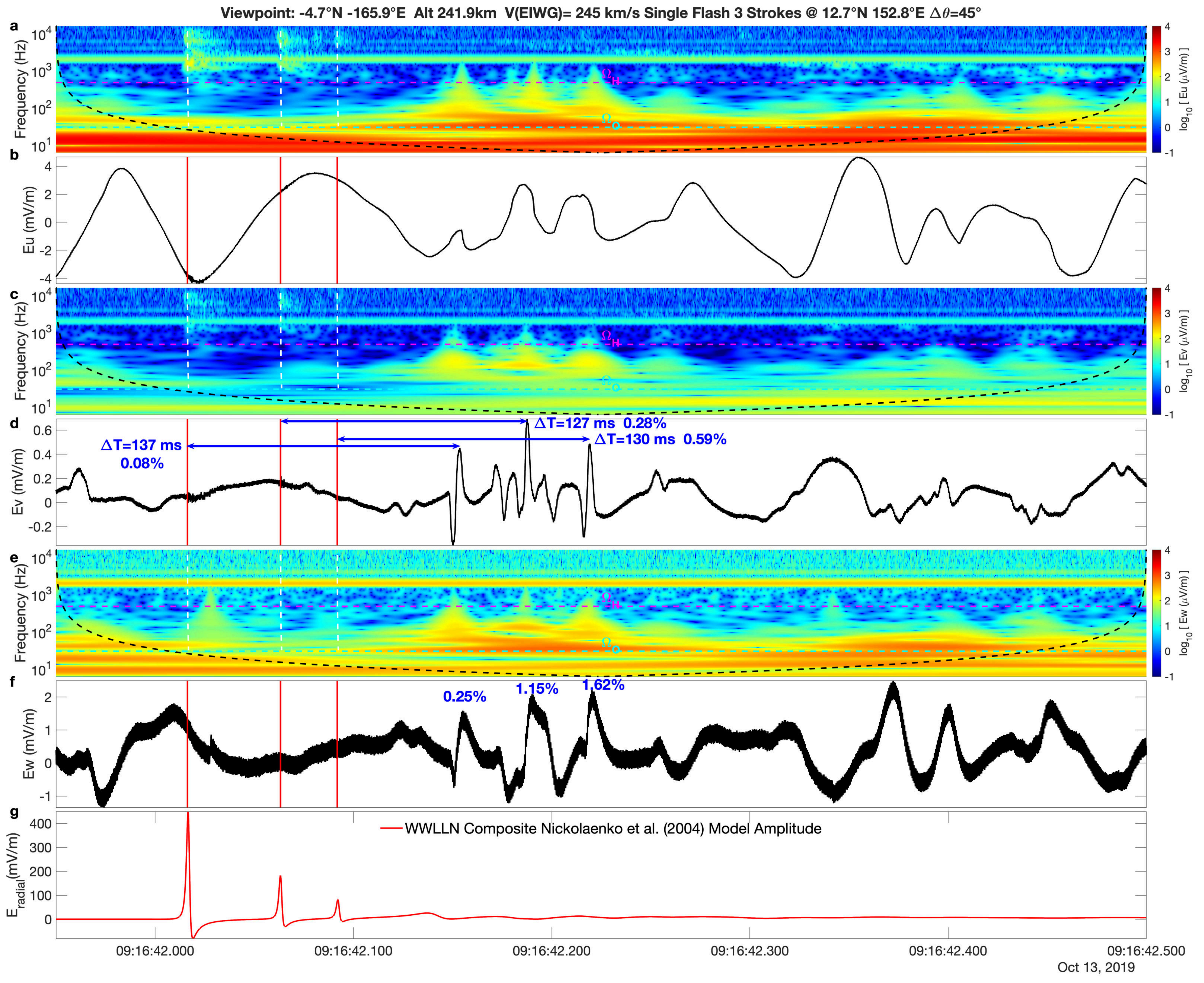

Viewpoint: -4.7°N -165.9°E Alt 241.9km V(EIWG)= 245 km/s Single Flash 3 Strokes @ 12.7°N 152.8°E Δθ=45°
a
Frequency (Hz)
Ω_H
Ω_O
$\log_{10}$ [Eu (μV/m)]
b
Eu (mV/m)
c
$\log_{10}$ [Ev (μV/m)]
d
ΔT=127 ms 0.28%
ΔT=130 ms 0.59%
ΔT=137 ms
0.08%
Ev (mV/m)
e
$\log_{10}$ [Ew (μV/m)]
f
0.25%
1.15%
1.62%
Ew (mV/m)
g
WWLLN Composite Nickolaenko et al. (2004) Model Amplitude
E_{radial}(mV/m)
09:16:42.000
09:16:42.100
09:16:42.200
09:16:42.300
09:16:42.400
09:16:42.500
Oct 13, 2019

Figure 3.

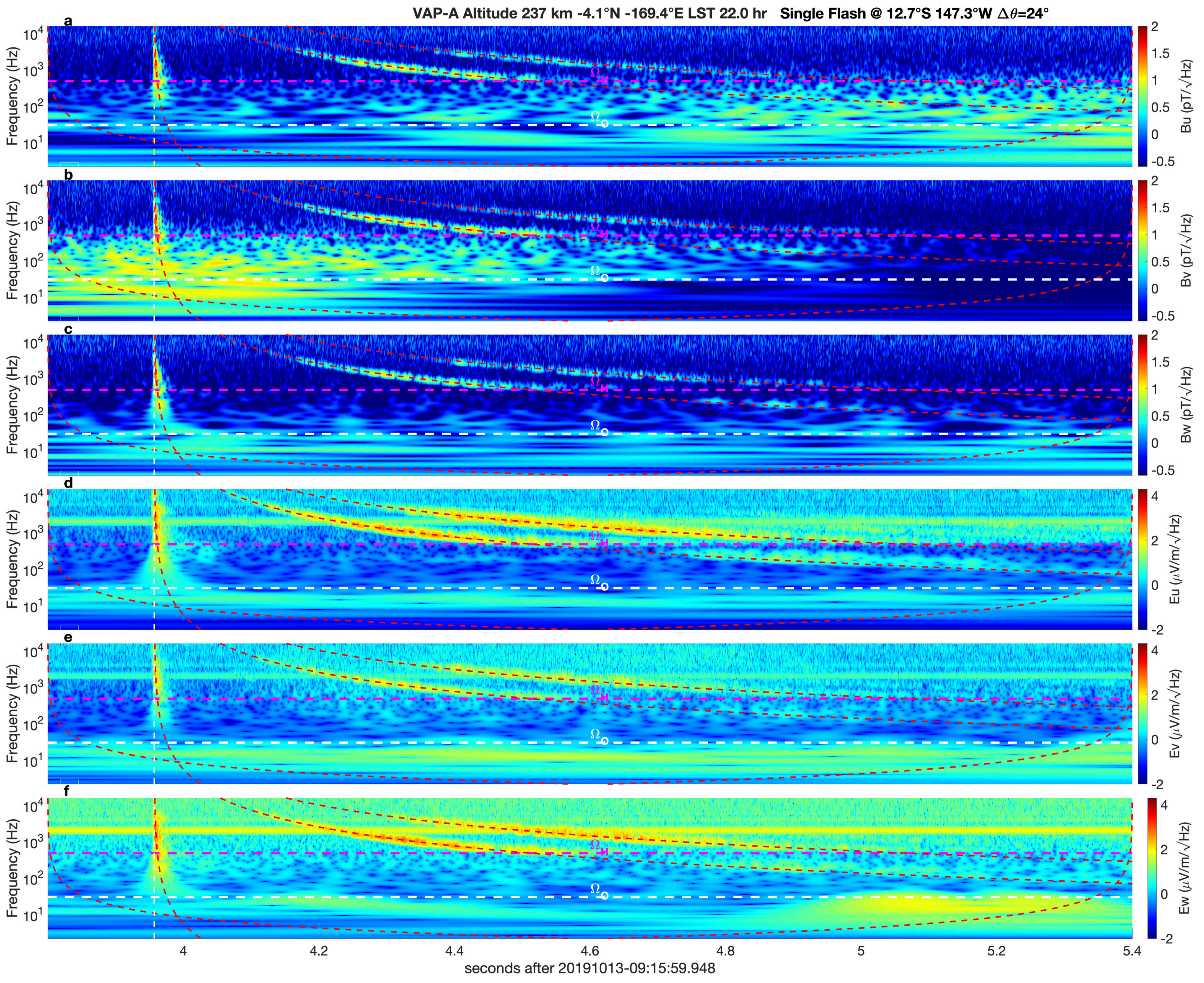
VAP-A Altitude 237 km -4.1°N -169.4°E LST 22.0 hr Single Flash @ 12.7°S 147.3°W Δθ=24°
a
b
c
d
e
f
Frequency (Hz)
Bu (pT/√Hz)
Bv (pT/√Hz)
Bw (pT/√Hz)
Eu (μV/m/√Hz)
Ev (μV/m/√Hz)
Ew (μV/m/√Hz)
seconds after 20191013-09:15:59.948

Figure 4.

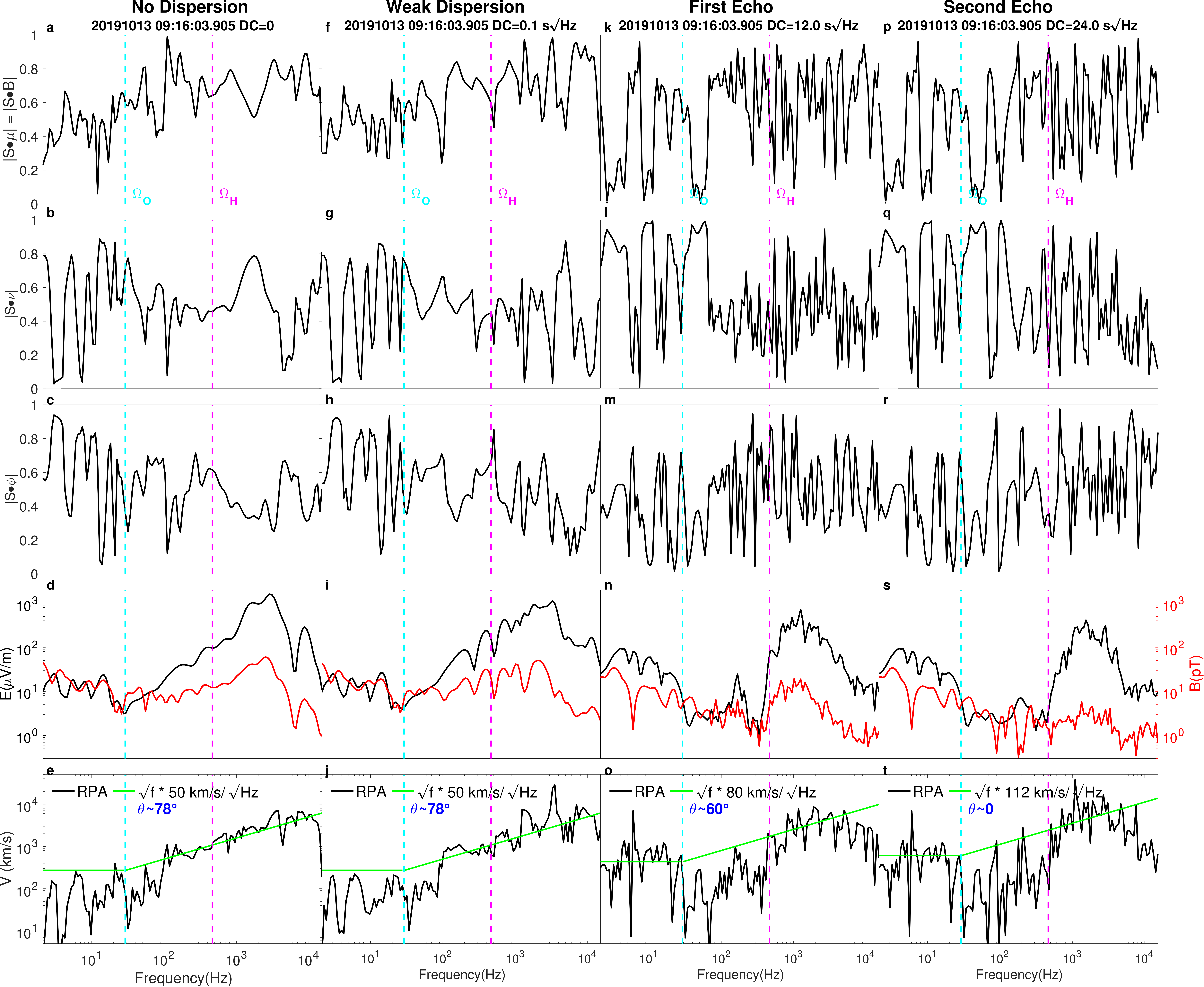

No Dispersion
Weak Dispersion
First Echo
Second Echo
a 20191013 09:16:03.905 DC=0
f 20191013 09:16:03.905 DC=0.1 s√Hz
k 20191013 09:16:03.905 DC=12.0 s√Hz
p 20191013 09:16:03.905 DC=24.0 s√Hz
|S•μ| = |S•B|
|S•ν|
|S•φ|
Ω_O
Ω_H
E(μV/m)
B(pT)
V (km/s)
RPA
√f * 50 km/s/ √Hz
θ~78°
√f * 80 km/s/ √Hz
θ~60°
√f * 112 km/s/ √Hz
θ~0
Frequency(Hz)

Figure 5.

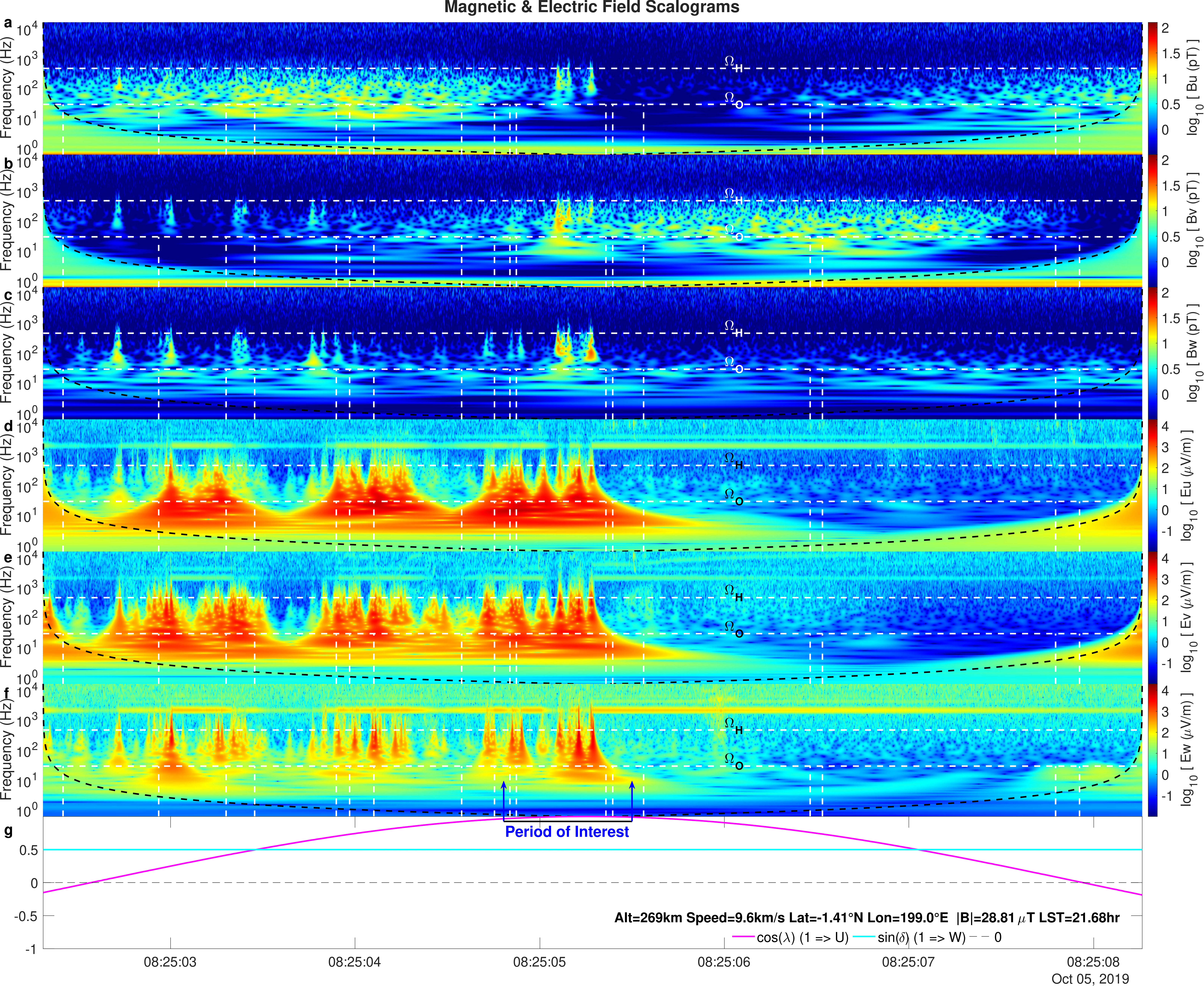

Magnetic & Electric Field Scalograms
a
b
c
d
e
f
g
Frequency (Hz)
log10 [Bu (pT)]
log10 [Bv (pT)]
log10 [Bw (pT)]
log10 [Eu (μV/m)]
log10 [Ev (μV/m)]
log10 [Ew (μV/m)]
Ω H
Ω O
Period of Interest
Alt=269km Speed=9.6km/s Lat=-1.41°N Lon=199.0°E |B|=28.81 μT LST=21.68hr
cos(λ) (1 => U)
sin(δ) (1 => W)
0
08:25:03
08:25:04
08:25:05
08:25:06
08:25:07
08:25:08
Oct 05, 2019

Figure 6.

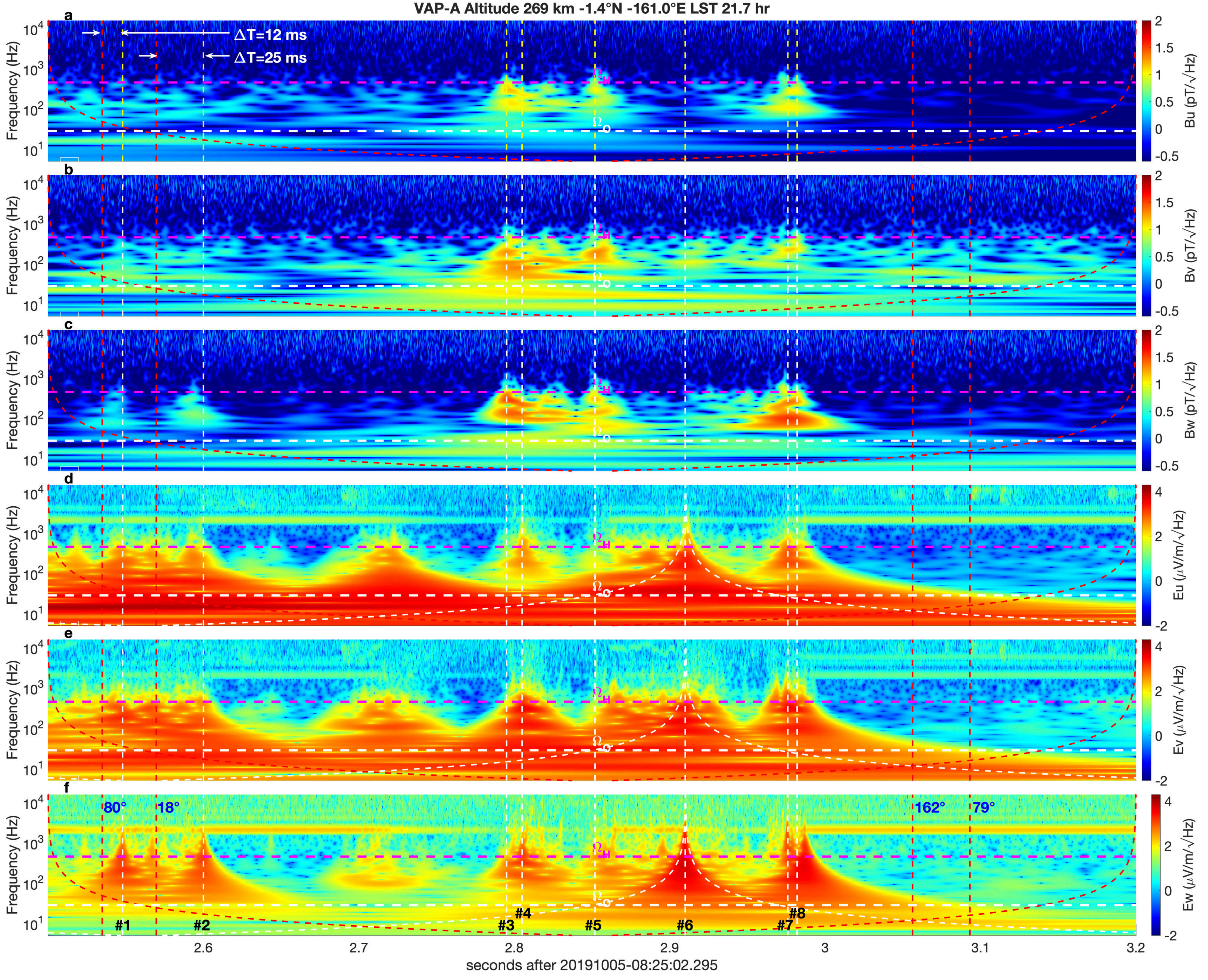

VAP-A Altitude 269 km -1.4°N -161.0°E LST 21.7 hr
a
b
c
d
e
f
ΔT=12 ms
ΔT=25 ms
Frequency (Hz)
Bu (pT/√Hz)
Bv (pT/√Hz)
Bw (pT/√Hz)
Eu (μV/m/√Hz)
Ev (μV/m/√Hz)
Ew (μV/m/√Hz)
Ω_H
Ω_O
80°
18°
162°
79°
#1
#2
#3
#4
#5
#6
#7
#8
seconds after 20191005-08:25:02.295

Figure 7.

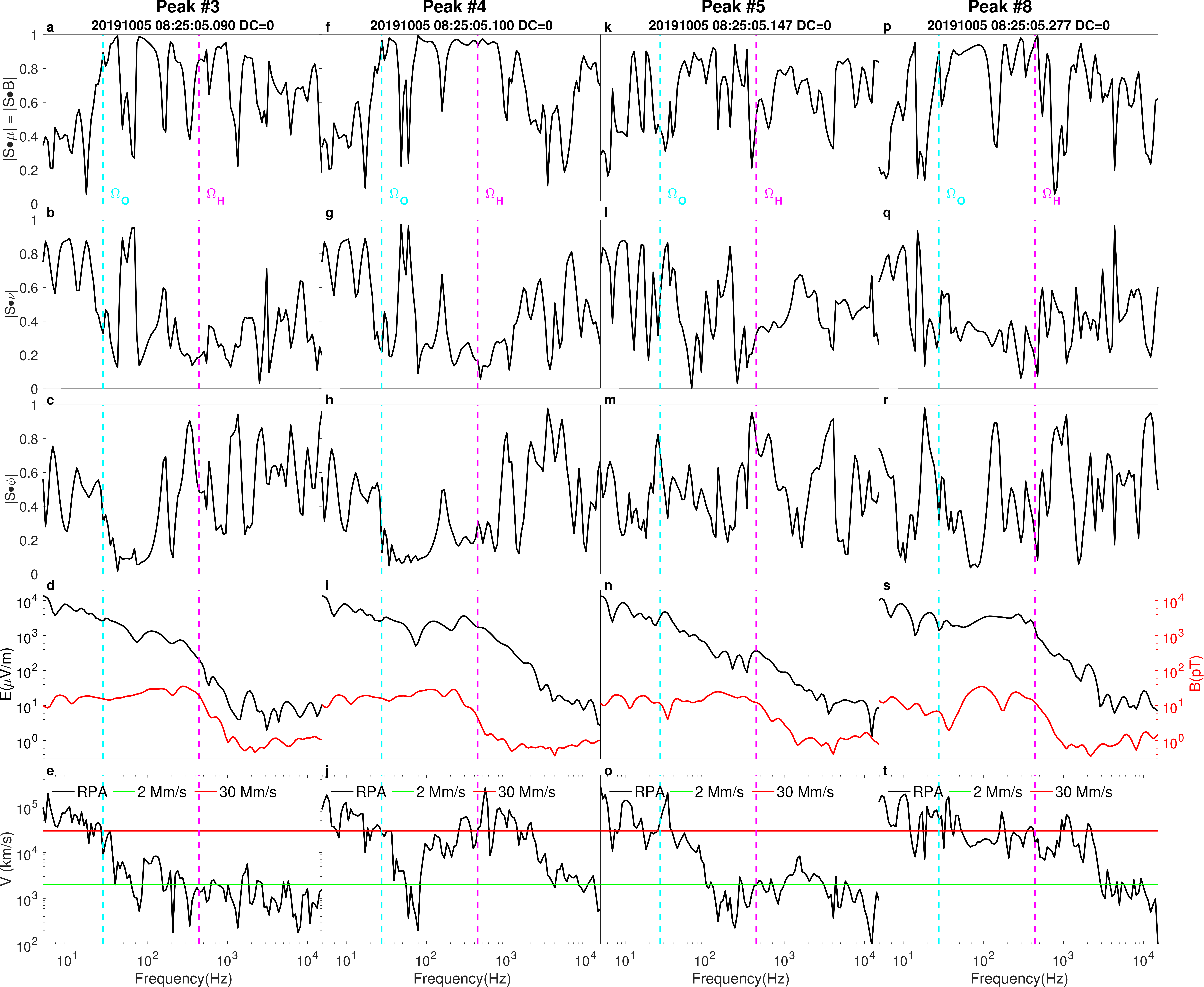

Peak #3
20191005 08:25:05.090 DC=0
Peak #4
20191005 08:25:05.100 DC=0
Peak #5
20191005 08:25:05.147 DC=0
Peak #8
20191005 08:25:05.277 DC=0
a
b
c
d
e
f
g
h
i
j
k
l
m
n
o
p
q
r
s
t
|S•μ| = |S•B|
|S•ν|
|S•φ|
E(μV/m)
B(pT)
V (km/s)
Ω_O
Ω_H
RPA
2 Mm/s
30 Mm/s
Frequency(Hz)

Figure 8.

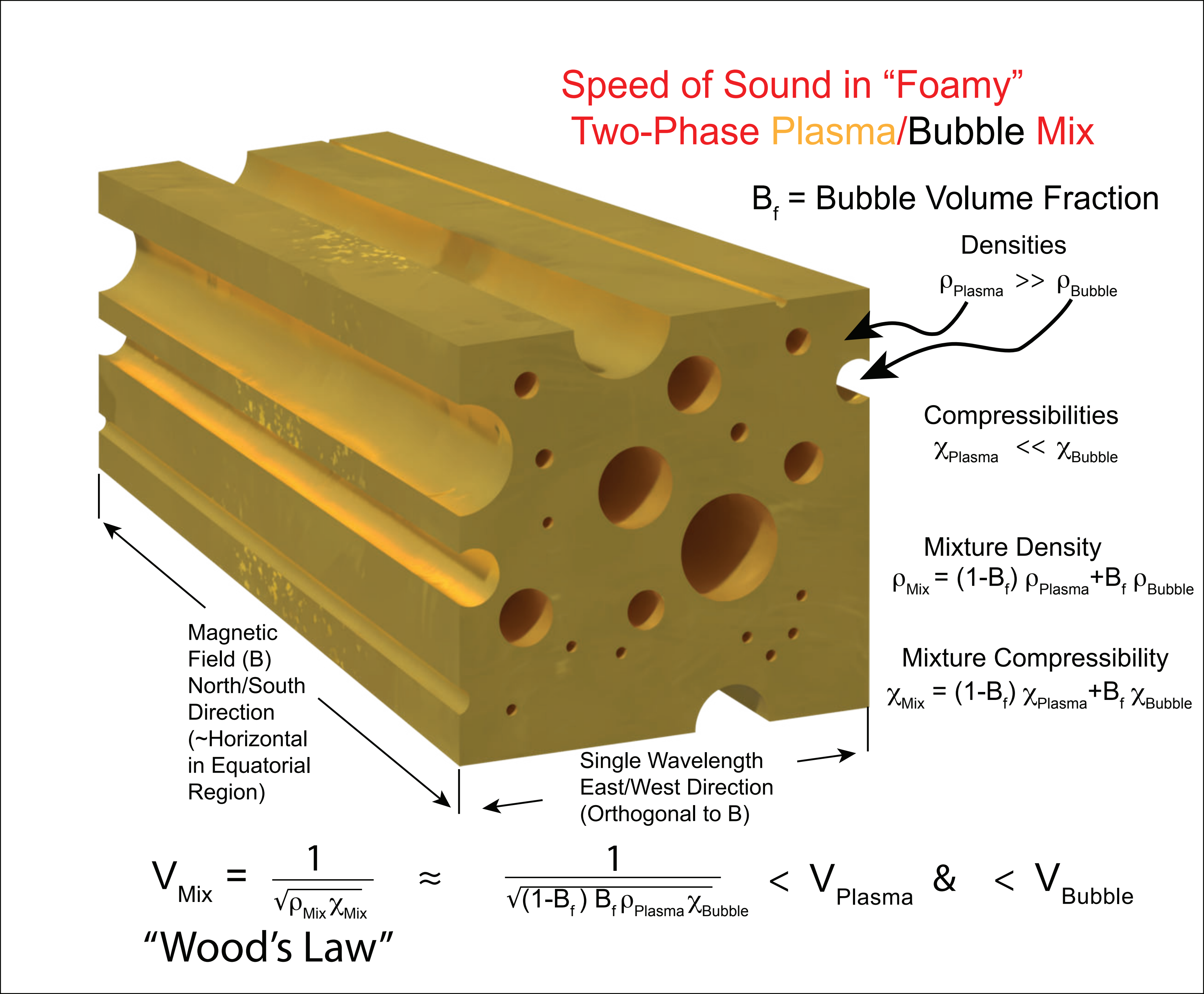

Speed of Sound in “Foamy”
Two-Phase Plasma/Bubble Mix
B_f = Bubble Volume Fraction
Densities
$\rho_{Plasma} >> \rho_{Bubble}$
Compressibilities
$\chi_{Plasma} << \chi_{Bubble}$
Mixture Density
$\rho_{Mix} = (1-B_f)\,\rho_{Plasma} + B_f\,\rho_{Bubble}$
Mixture Compressibility
$\chi_{Mix} = (1-B_f)\,\chi_{Plasma} + B_f\,\chi_{Bubble}$
Magnetic Field (B) North/South Direction (~Horizontal in Equatorial Region)
Single Wavelength East/West Direction (Orthogonal to B)
$V_{Mix} = \frac{1}{\sqrt{\rho_{Mix}\chi_{Mix}}} \approx \frac{1}{\sqrt{(1-B_f)\,B_f\,\rho_{Plasma}\,\chi_{Bubble}}} < V_{Plasma}\ \&\ < V_{Bubble}$
“Wood’s Law”

Figure 9.

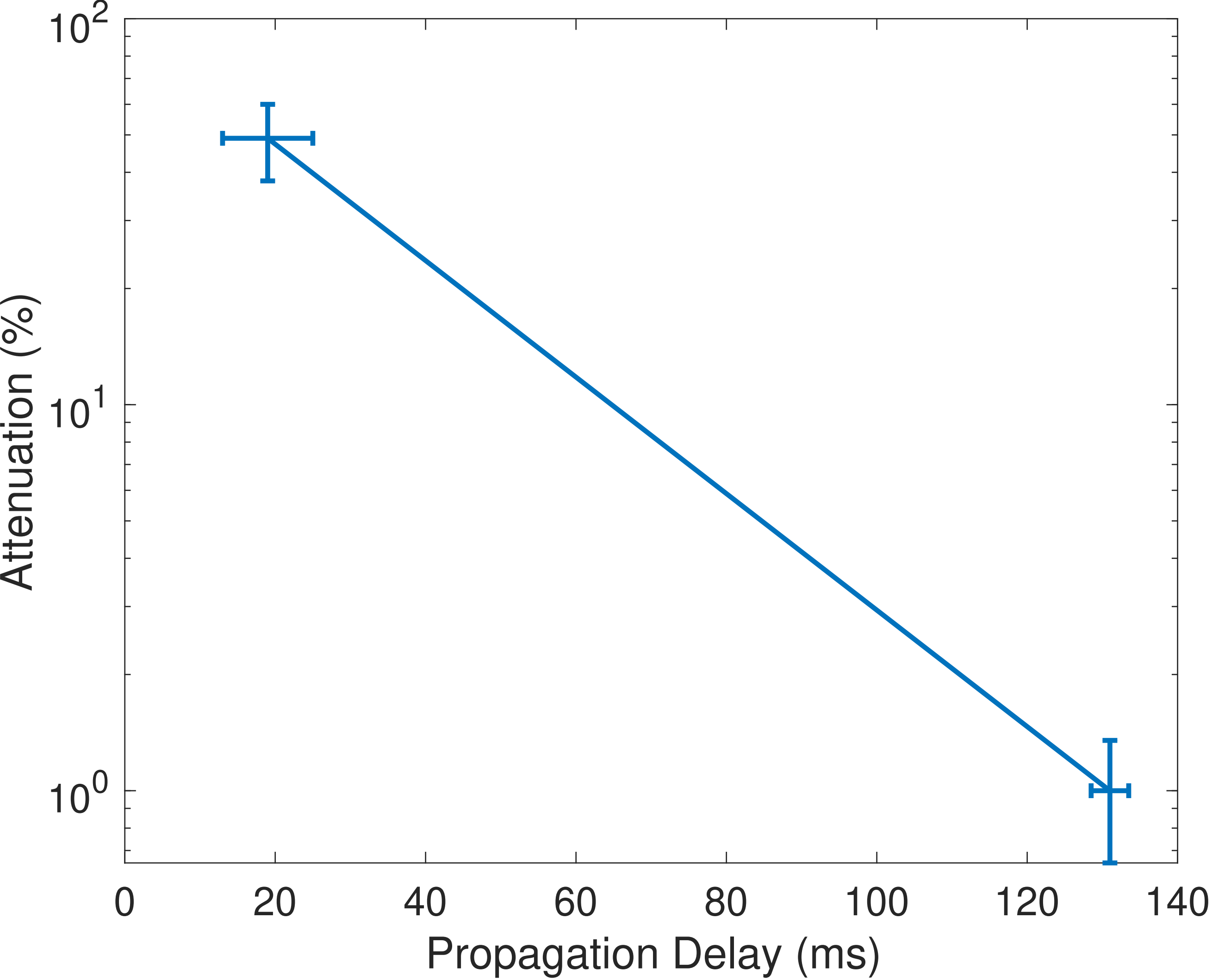

10^2
10^1
10^0
Attenuation (%)
0
20
40
60
80
100
120
140
Propagation Delay (ms)

Journal of Geophysical Research: Space Physics

Supporting Information for

Observations of the Roots of Plasma Bubbles: Are They Sometimes Foamy?

Charles L. Bennett[1]

[1]Retired, Lawrence Livermore National Laboratory.

Contents of this file

Figures S1 to S12

Introduction

The first nine of these figures provide supporting evidence for the existence of occasional "precursors" to the unusual nearly dispersionless spikes observed in scalograms while the Van Allen probe is located within the root of a plasma bubble. The layout of each of these nine figures follows that of Figure 1 and 2 in the main article.

The last three of these figures provide the supporting evidence for the group velocity of 245 km/s for the propagation of lightning generated EMPs through the Earth-Ionosphere waveguide (EIWG) at the time of the data shown in Figure 2 of the main article. In each of these three figures, the scalograms and time resolved plots of the two horizontal magnetic field fluctuations observed at one of the WERA ground stations are shown. The appearance times for lightning generated (LG) pulses from the three lightning strikes are indicated on the plots by red vertical lines.

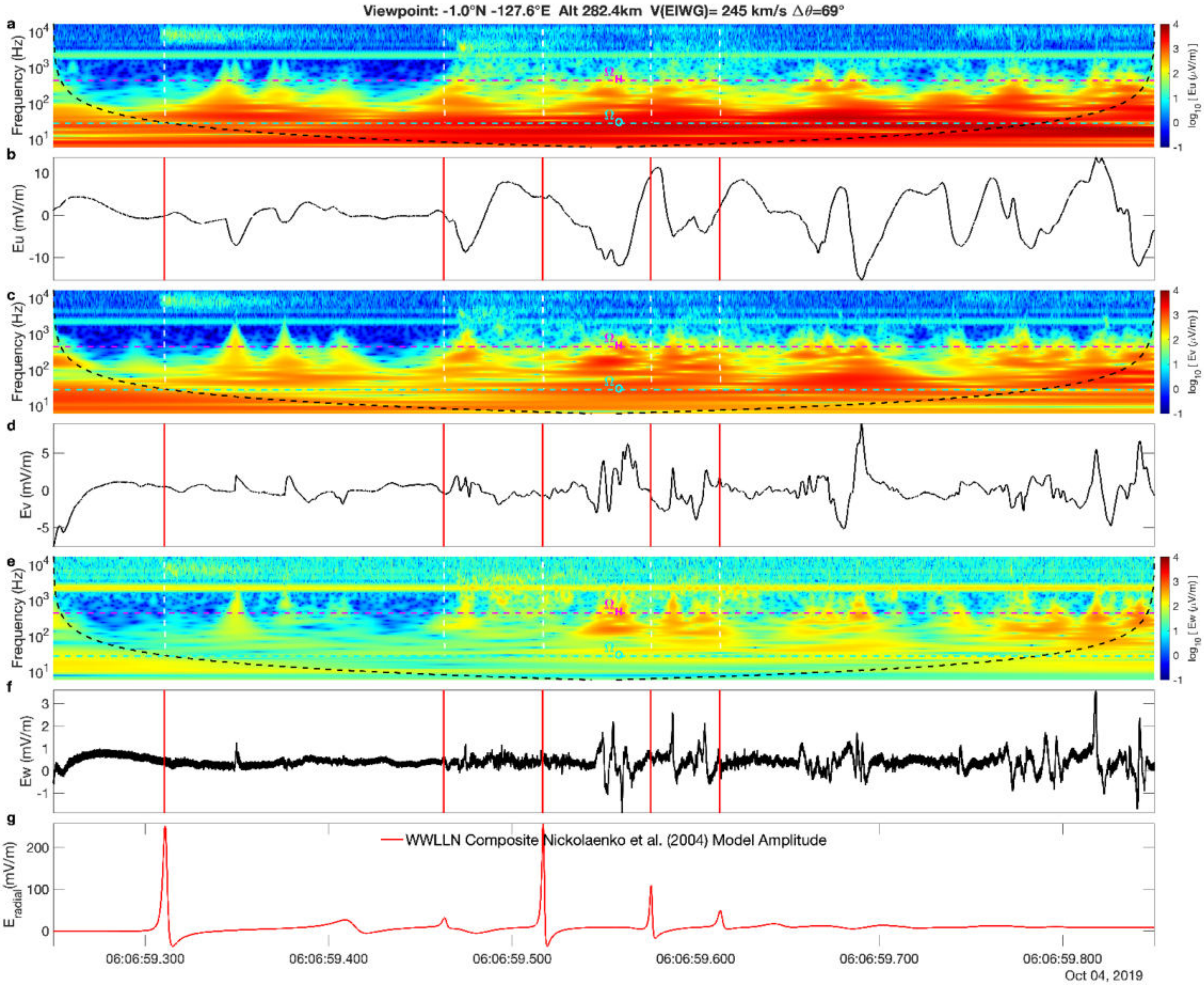

Figure S1. The layout of this figure is the same as Figures 1 & 2 in the main article. Scalograms (in **a**, **c**, and **e**) and time resolved plots (**b**, **d**, and **f**) of the electric field components are shown for a period while VAP-A passes through the root of a plasma bubble. In **g** the radial electric field from all WWLLN detected lightning strokes within this time interval using the (Nickolaenko et al., 2004) model is plotted. This case includes five distinct lightning strokes. The first of these has significant "precursor" activity in Eu and Ev between 3 kHz and 10 kHz, but the presence of corresponding Ew activity is obscured by the high noise level. Only the first two strokes are sufficiently well isolated that their precursors can be seen clearly aligned with the LG pulse arrival times. Because so many spikes appear in the scalograms, it is difficult to properly correlate specific spikes with their precursors.

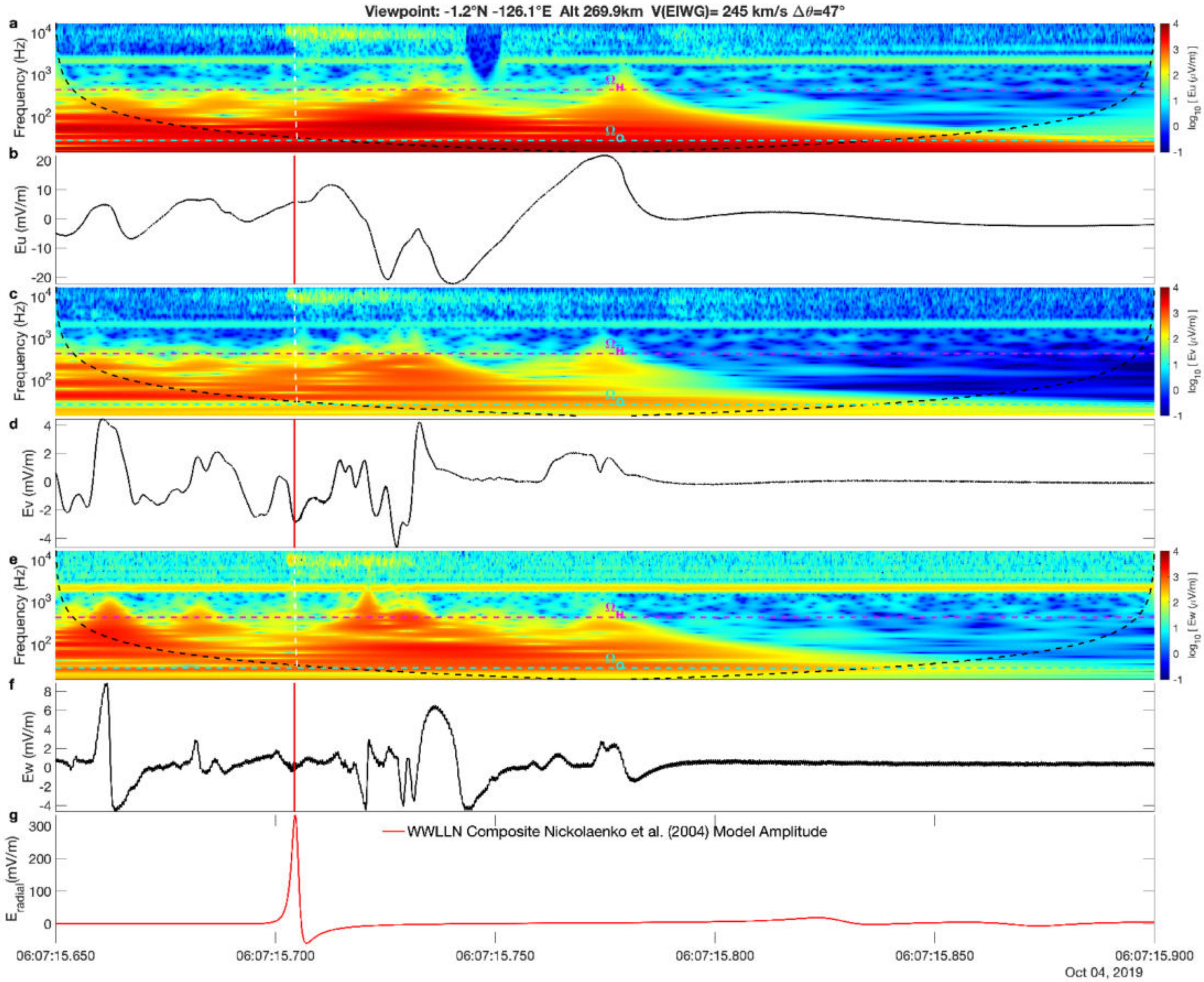

Figure S2. The layout of this figure is the same as the previous figure. In this case, although the precursor timing is clear, it is very unclear which, if any, of the spikes in the scalograms are associated with it.

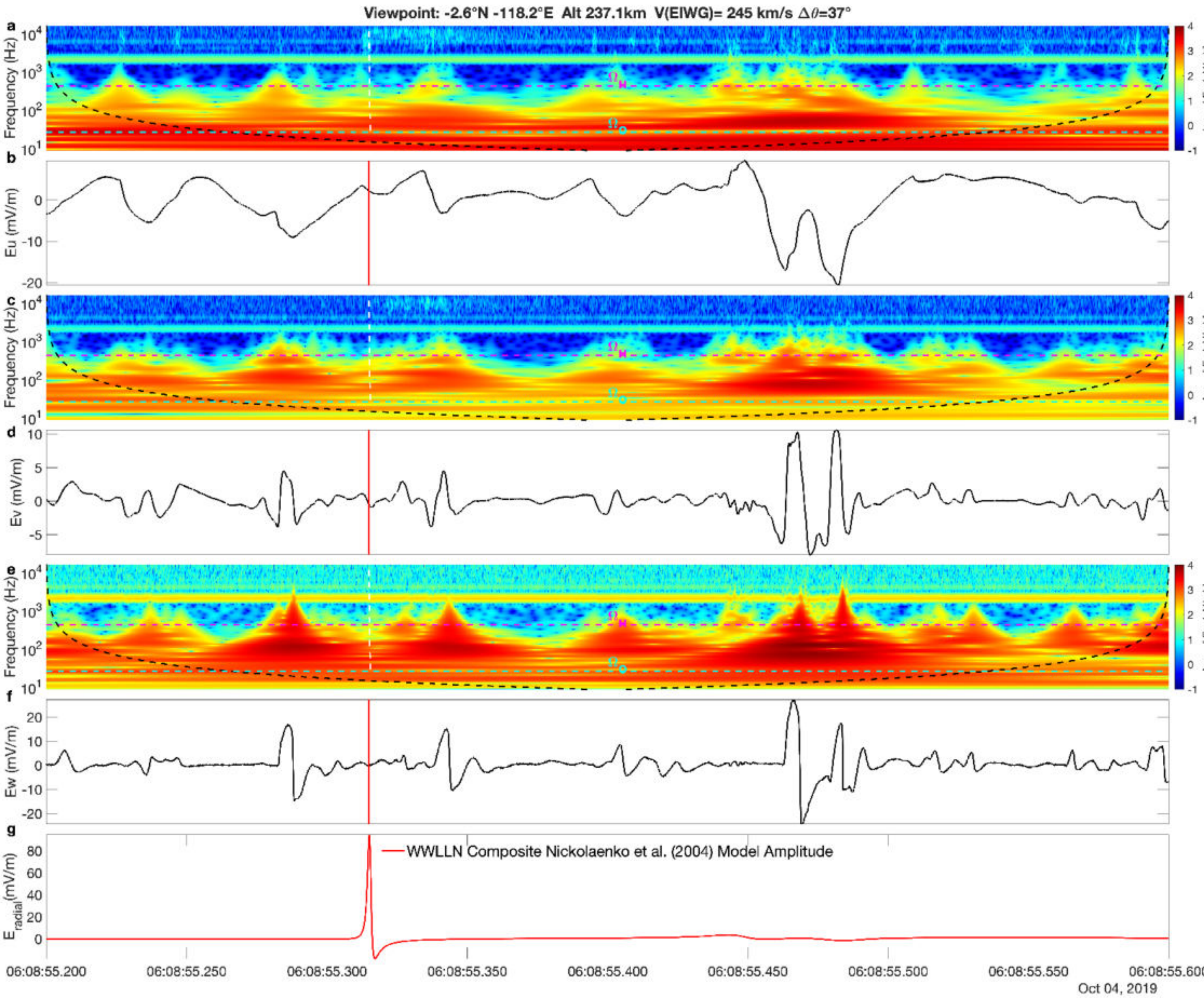

Figure S3. The layout of this figure is the same as the previous figure. In this case, although the precursor timing is clear, it is very unclear which, if any, of the spikes in the scalograms are associated with it.

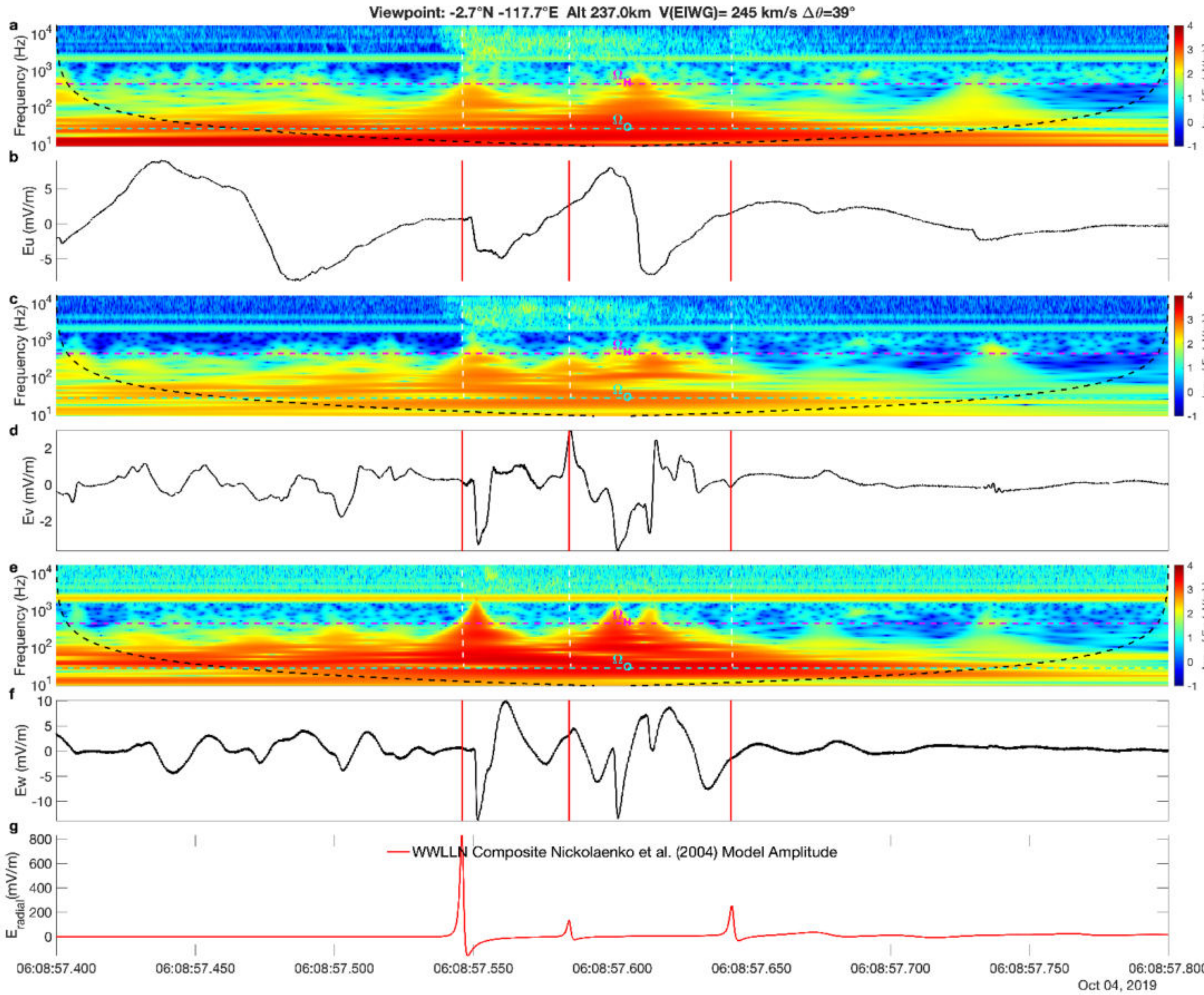

Figure S4. The layout of this figure is the same as the previous figure. In this case, although the precursor timing is clear for the first and third strokes, it is very unclear which, if any, of the spikes in the scalograms are associated with them.

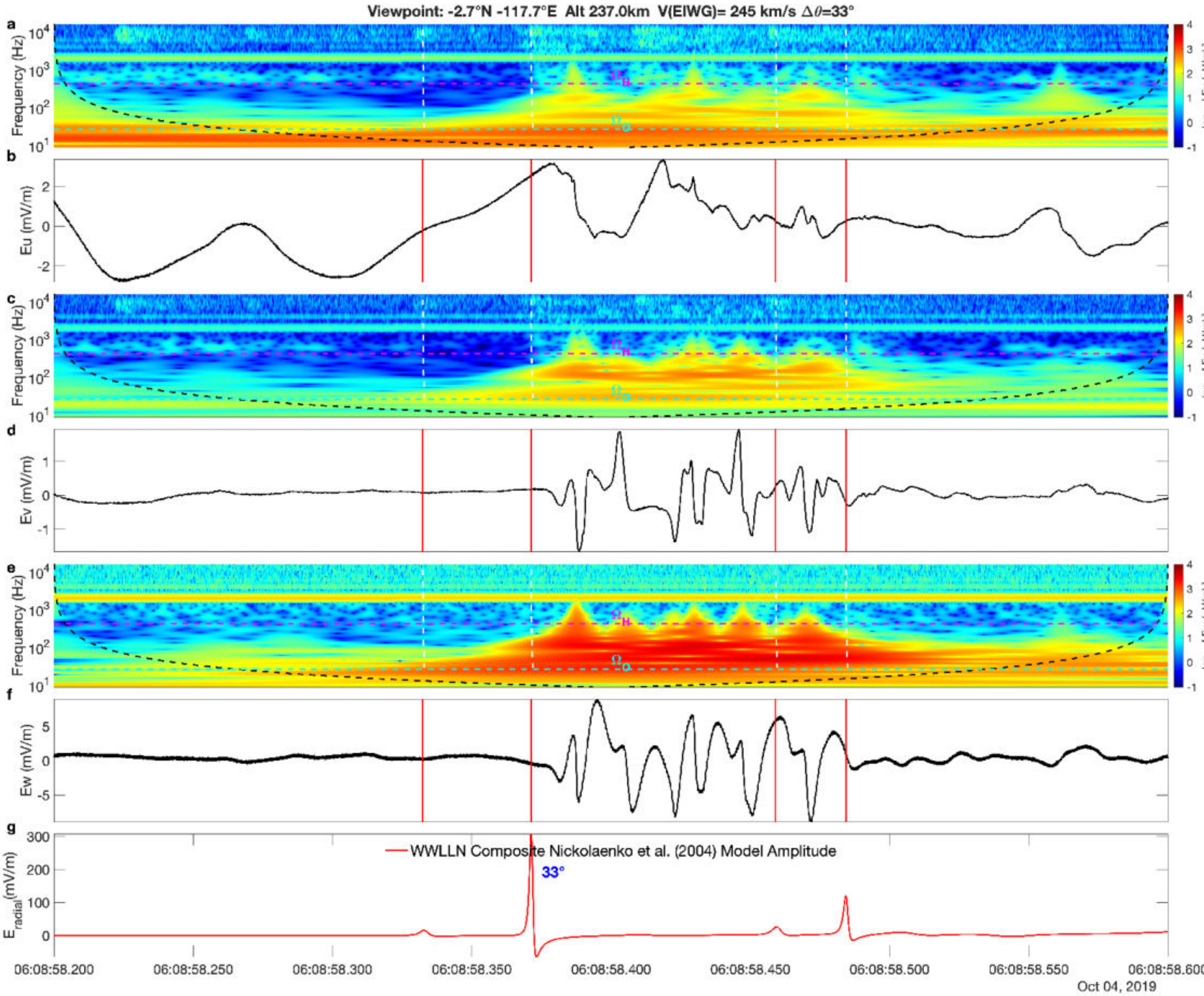

Figure S5. The layout of this figure is the same as the previous figure. In this case, although the precursor timing is clear for the first and second strokes, it is very unclear which, if any, of the spikes in the scalograms are associated with them.

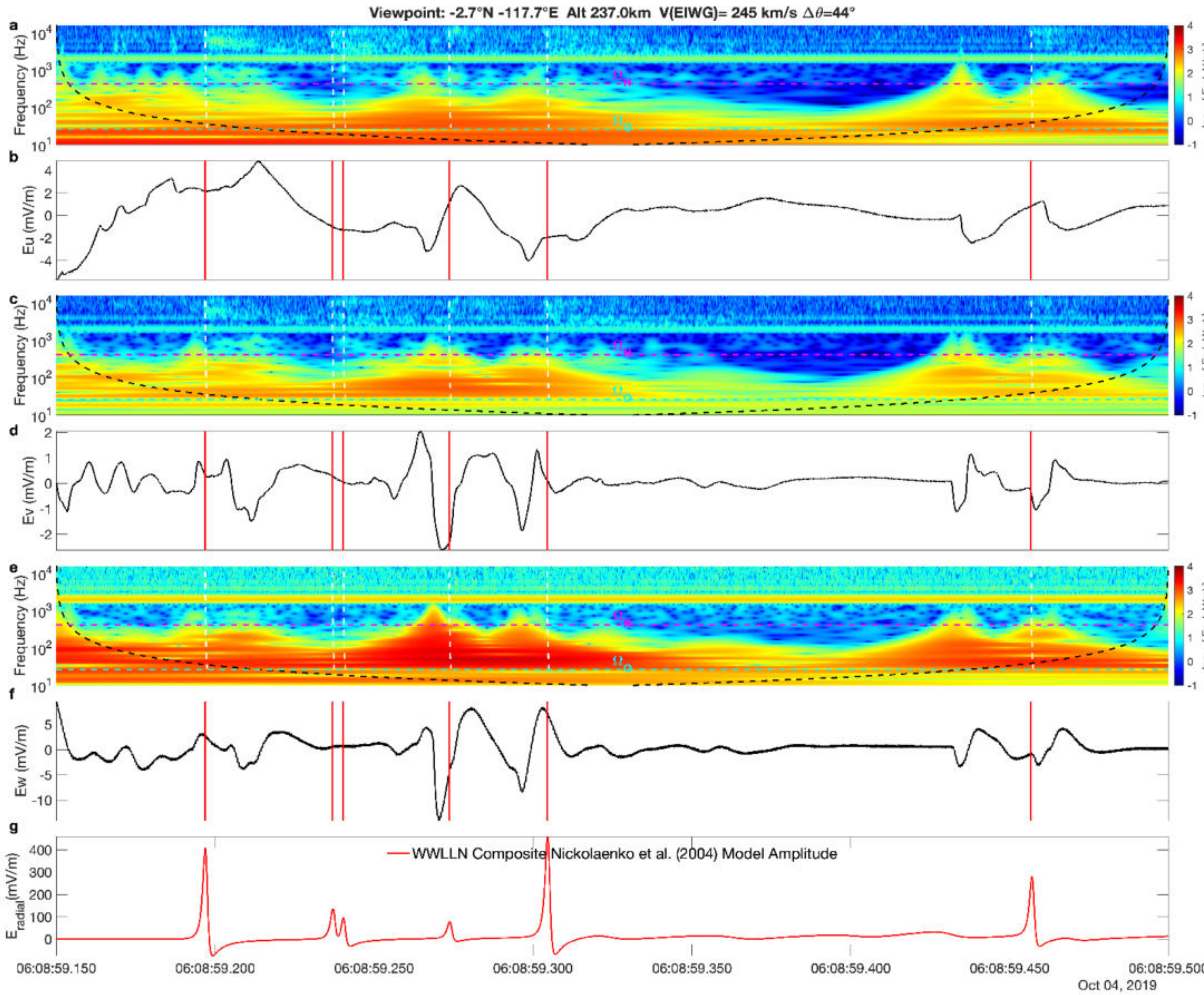

Figure S6. The layout of this figure is the same as the previous figure. In this case, although the precursor timing is clear for five of the six strokes, it is very unclear which, if any, of the spikes in the scalograms are associated with them.

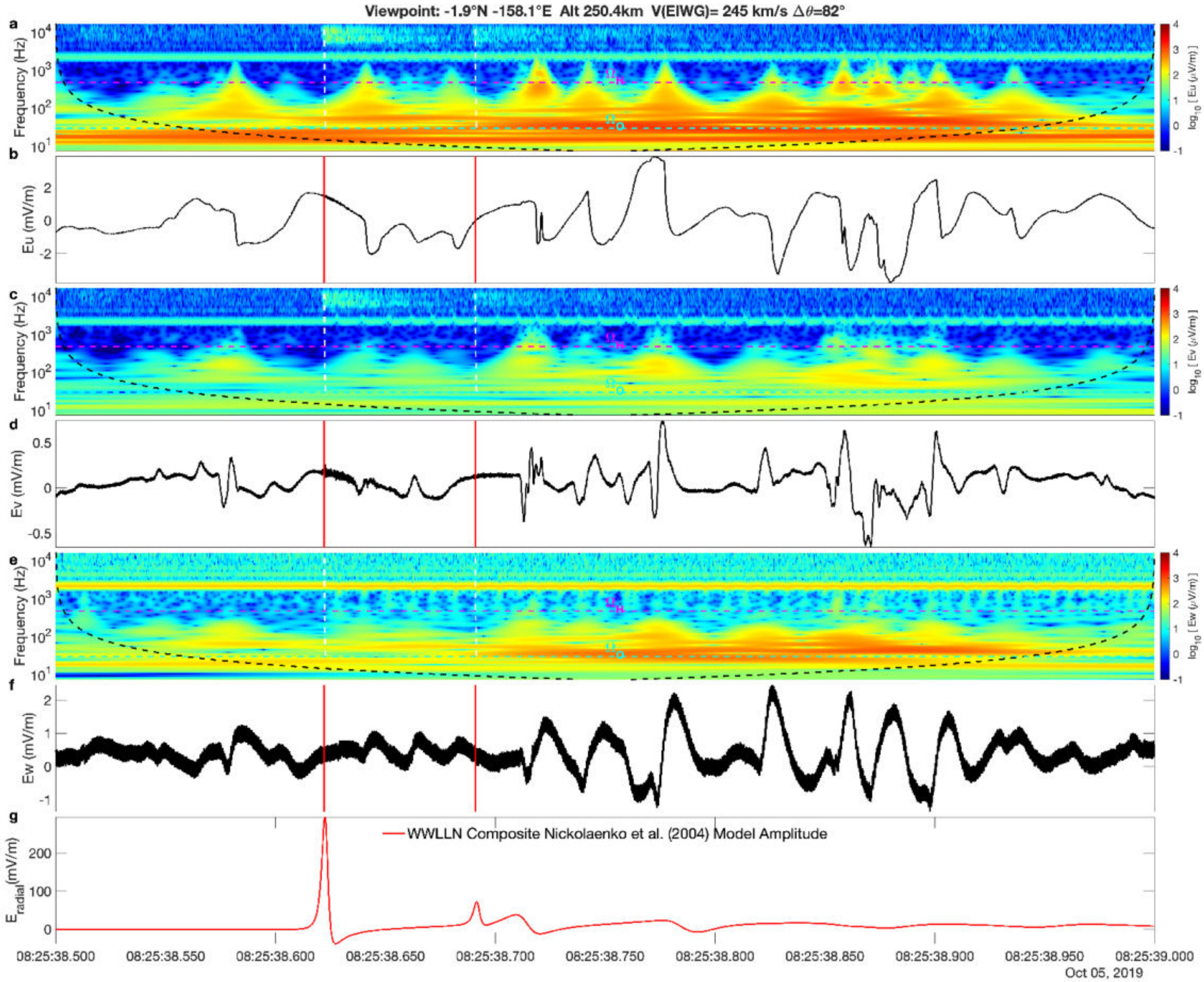

Figure S7. The layout of this figure is the same as the previous figure. In this case, although the precursor timing is clear for both strokes, it is very unclear which, if any, of the spikes in the scalograms are associated with them.

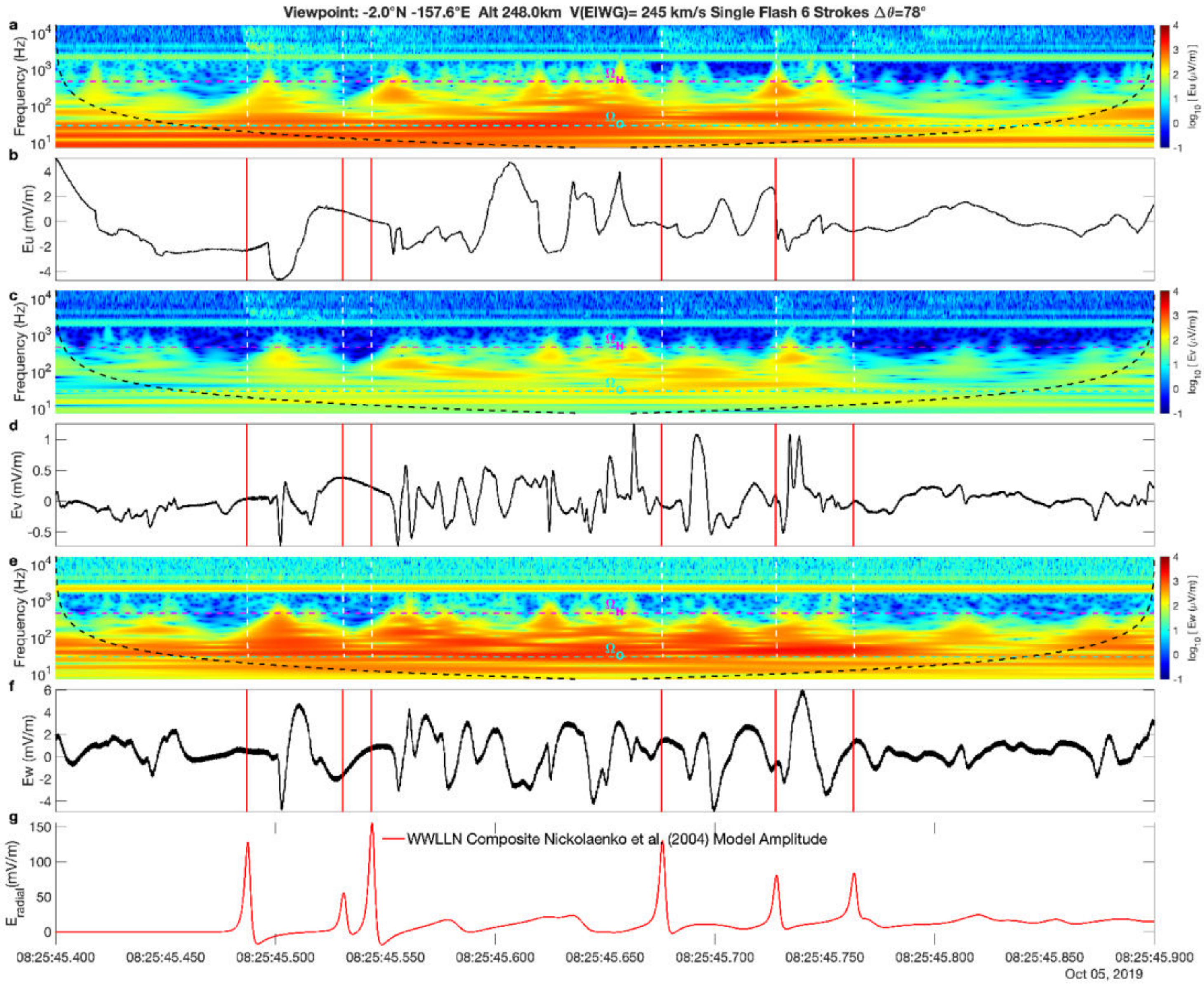

Figure S8. The layout of this figure is the same as the previous figure. In this case, although the precursor timing is clear for strokes #1, #4, #5 and #6, it is very unclear which, if any, of the spikes in the scalograms are associated with them.

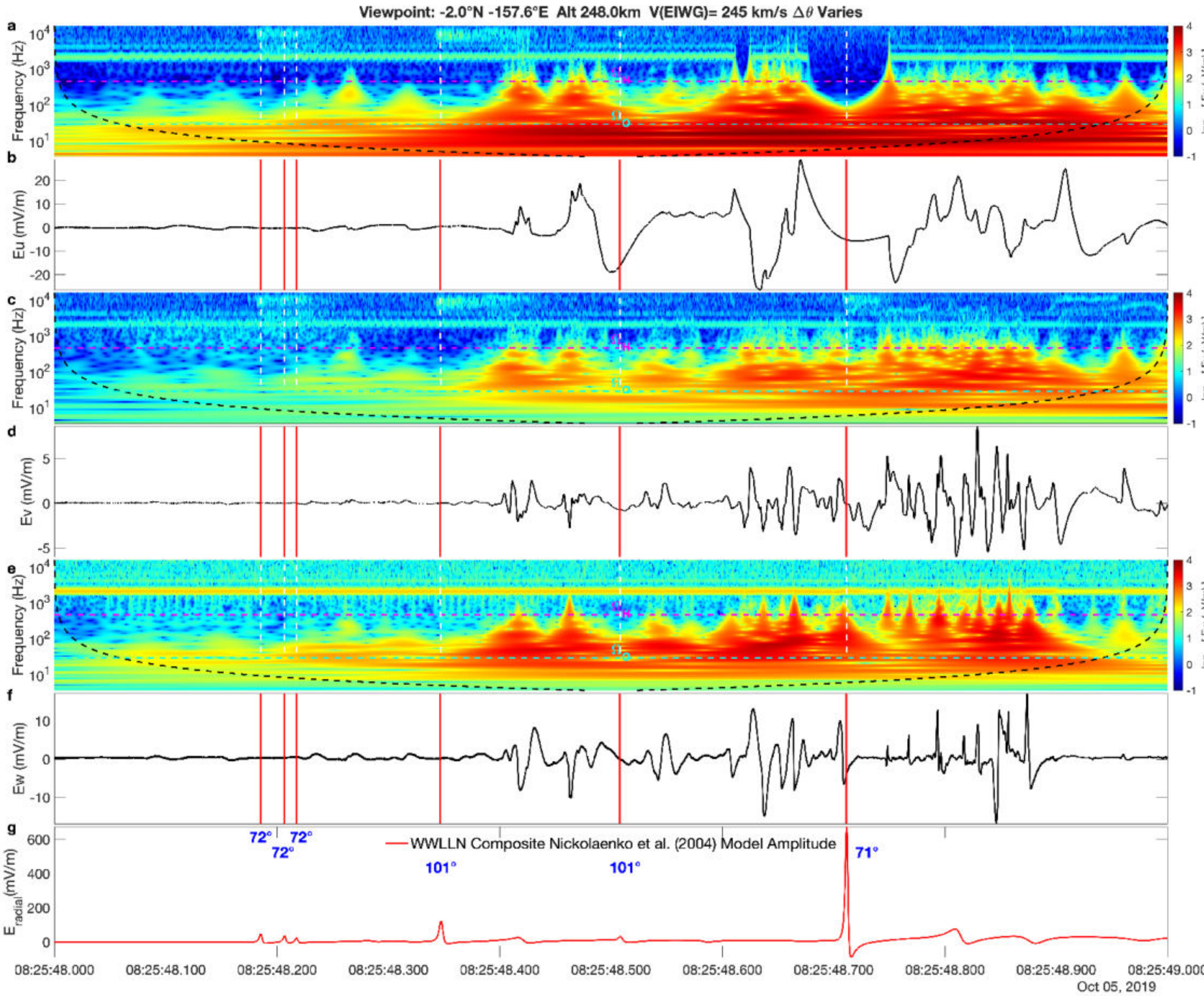

Figure S9. The layout of this figure is the same as the previous figure. In this case, although the precursor timing is clear for strokes #1, #4, #5 and #6, it is very unclear which, if any, of the spikes in the scalograms are associated with them.

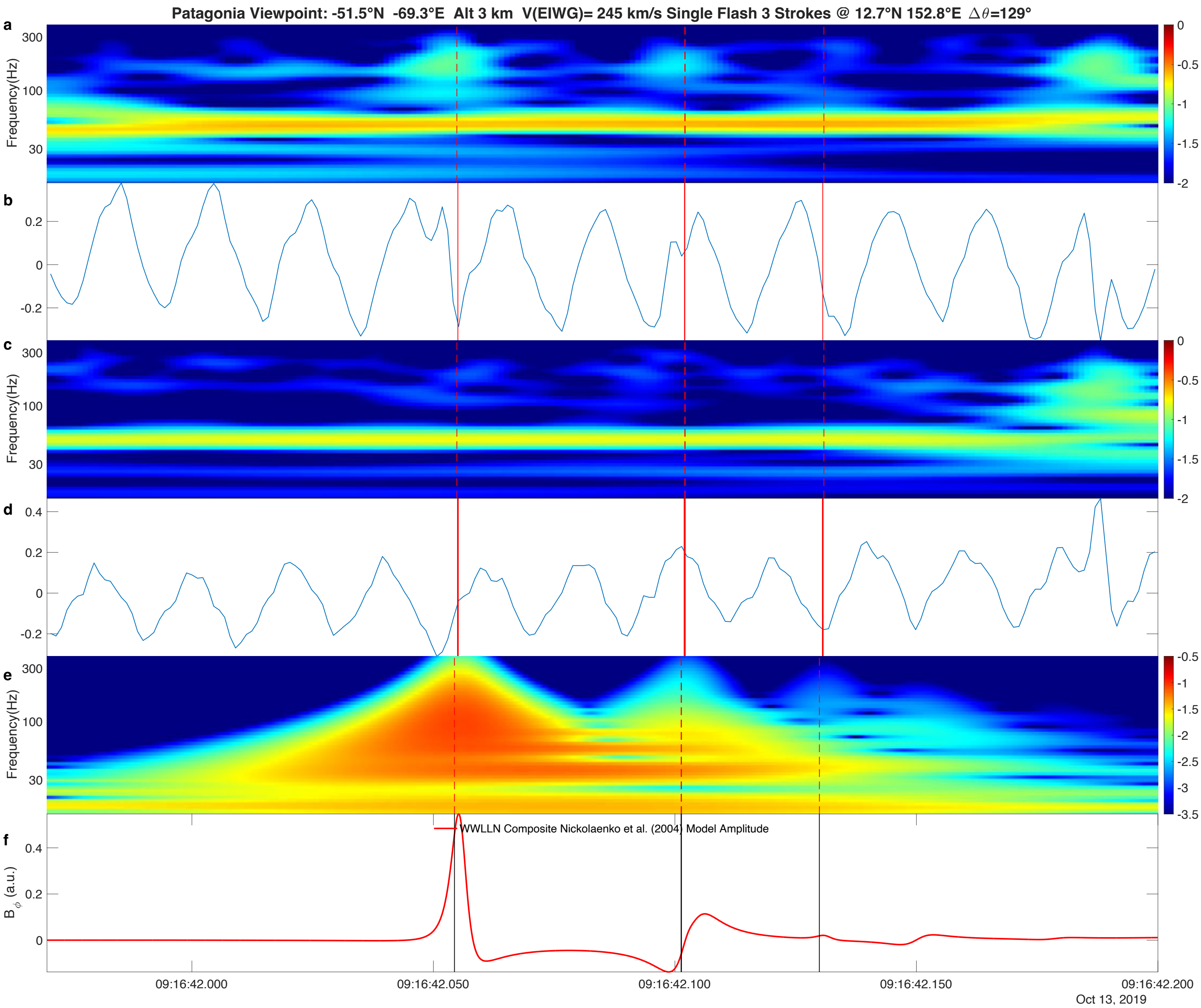

Figure S10. Scalograms for the two WERA magnetic field components observed at the Patagonia site, along with their time resolved values are shown for the 0.23 s interval centered around the time of the three lightning strokes discussed in Figure **2** of the main article. In (**a** and **c**) scalograms for the North/South (NS) and East/West (EW) components of magnetic field are shown. In (**b** and **d**) the NS and EW magnetic fields are plotted as a function of time. In (**f**) the summation of the azimuthal magnetic field contributions from the three WWLLN detected strokes during this time using the (Nickolaenko et al., 2004) model is plotted. In (**e**) the scalogram of the temporal function plotted in (**f**) is shown. Red dashed or solid lines show the arrival time assuming the propagation speed of 245 km/s at the subsatellite location for each of the three lightning stroke pulses.

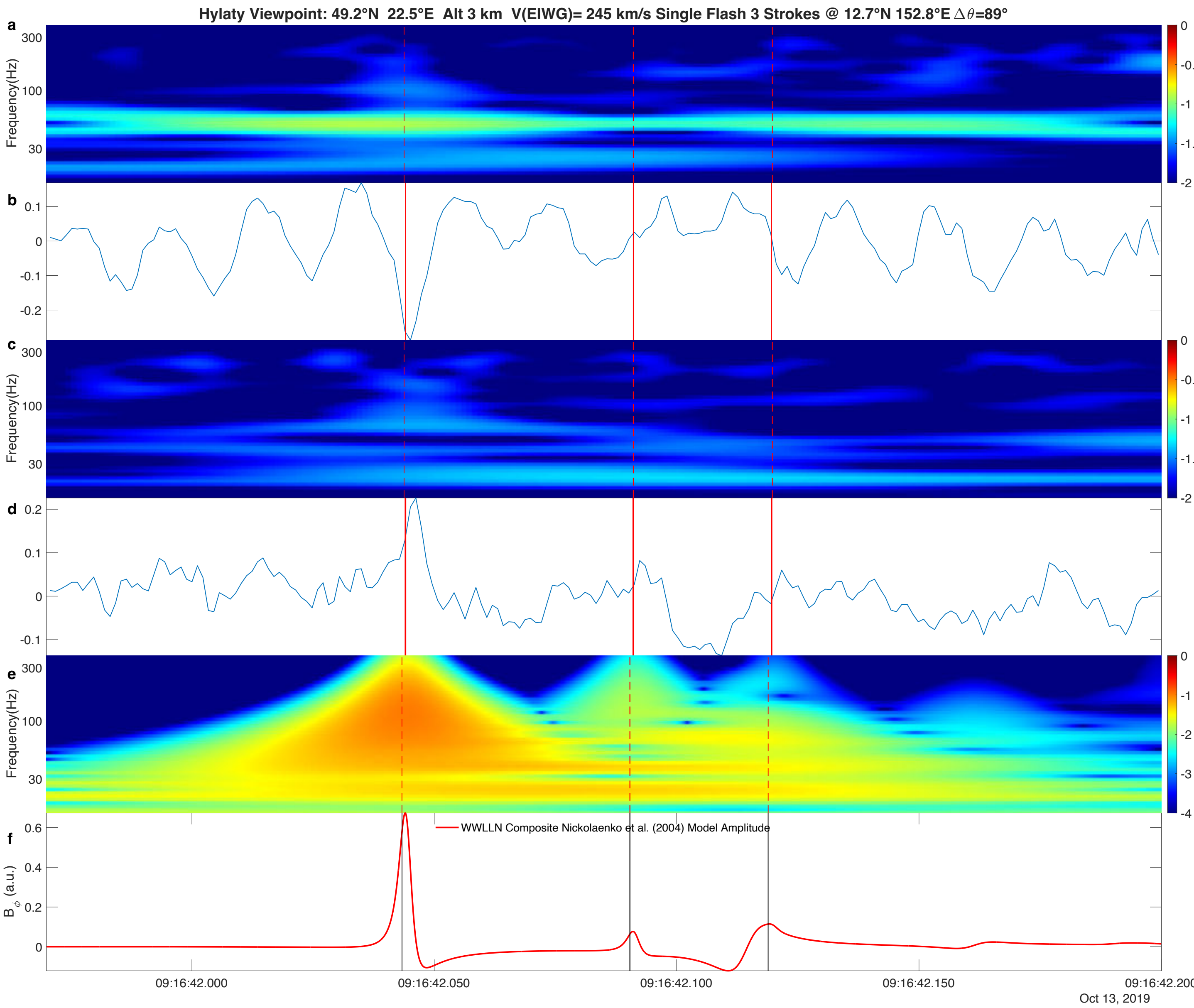

Figure S11. Scalograms and time resolved values for the two WERA magnetic field components observed at the Hylaty site are shown with the same layout as the previous figure.

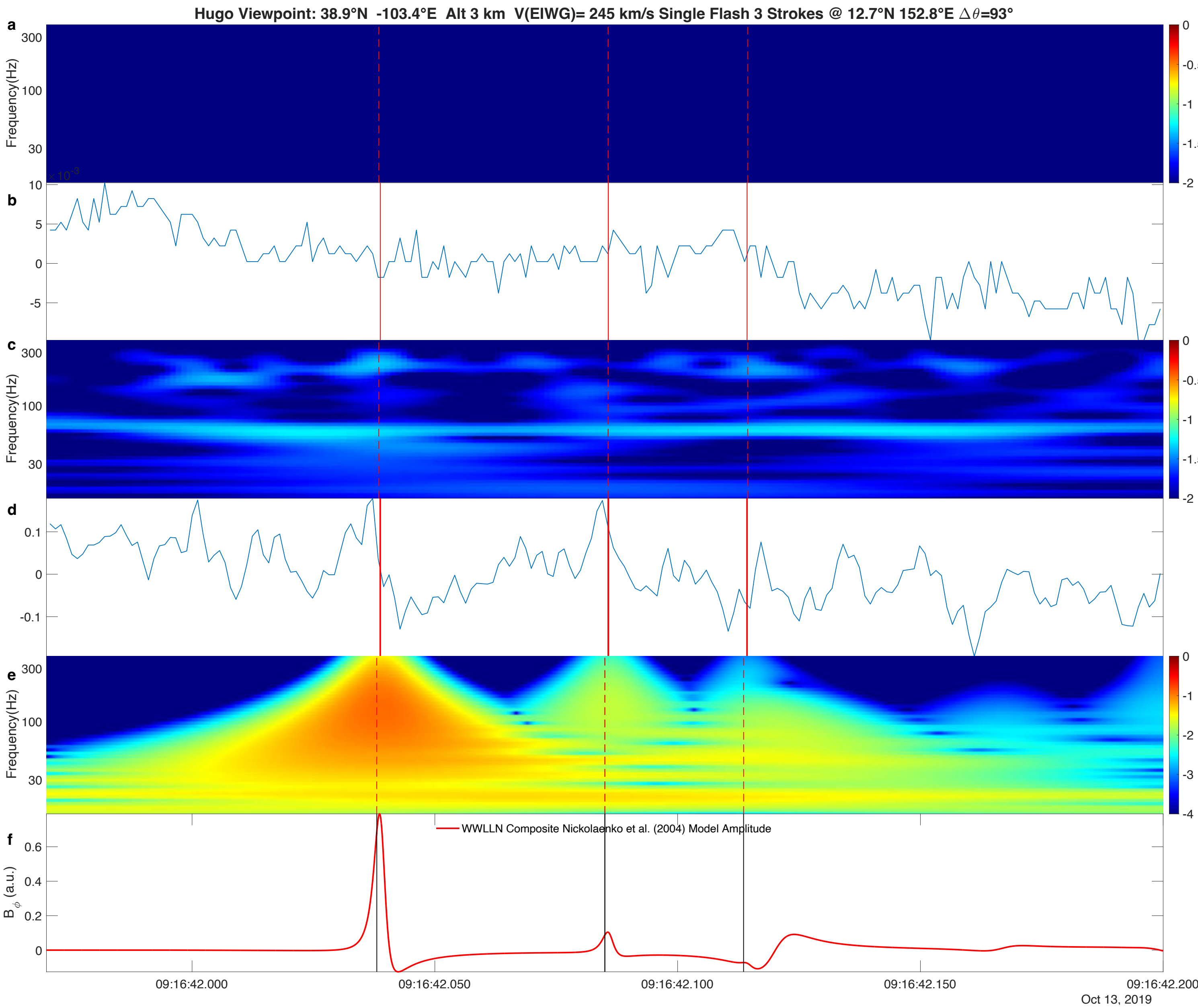

Figure S12. Scalograms and time resolved values for the two WERA magnetic field components observed at the Hugo site are shown with the same layout as the previous figure. In this case, the NS magnetic field components were noisy and not meaningful.